DESIGN AND FABRICATION OF 1-D, 2-D PHOTONIC CRYSTALS AND METASURFACE BASED PERFECT LIGHT ABOSORBERS

A Thesis

by

ARUN BHASKAR

Submitted to the Office of Graduate and Professional Studies of
Texas A&M University
in partial fulfillment of the requirements for the degree of

MASTER OF SCIENCE

Chair of Committee,	Sy-Bor Wen
Committee Members,	Jerald A Caton
	Adonios Karpetis
Head of Department,	Andreas A Polycarpou

December 2016

Major Subject: Mechanical Engineering

ABSTRACT

Perfect light absorbers are devices which absorb all the light that is incident up on it at a particular frequency. Perfect light absorbers find applications in designing efficient solar absobers, thermophotovoltaic energy conversion systems and stealth technologies. Two methods to realize prefect light absorbers are investigated in this thesis; one using 2-D metallic photonic crystals and using metasurface based absorbers.

Photonic crystals have periodic variation of dielectric constant at a subwavelength scale of the light.These periodic variation of dielectric constant lead to the formation of photonic band gaps in these materials. The two dimensional metallic photonic crystal consist of square array of cylindrical cavities on a tantalum metal surface. These cavities on the metal surface couple to the incident electromagnetic radiation and lead to enhanced absorption. The effect of design parameters namely choice of metal, radius, depth and period of the cylinders on the absorption of light is studied and then an optimum design providing peak emissivity at 3.5 μm is arrived at and fabricated.

Metasurface based aborbers on the other hand are composite materials with artifical permeability and permitivity. A qualitative picture for creating the artifical permitivity and permeability formation in this material is given in this thesis, with a contrast to the atomic scale resonance to explain the optical properties of these materials. We show how by controlling the design of the electric ring resonator and split ring resonators we can the create perfect light absorption in these metasurface absorbers. We then discuss the equivalence of the complimentary electric ring resonators

DEDICATION

Matha, Pitha, Guru, Deivam (Mother, Father, Teacher, God)

Vijayalakshmi K D

A K Bhaskaran

Dr. Sy-Bor Wen

ACKNOWLEDGEMENTS

I thank Dr. Wen for all the support extended to me during my masters study. I will always be grateful to you for introducing me to this wonderful filed of electromagnetism. I am indebted to Yu, Hongie, Daniel and Kevin Ly for all those discussion which helped me in lot of decisions I made through out this work.

I would like to thank Larry Rehn, Jim Gardner, Edward Gonzales, Michael Babb and many users of the TAMU Aggiefab for their help extended during the fabrication of the metallic photonic crystals. I also acknowledge the assistance of Dr. Ping Luo and Derek Rodriguez of Texas AM Supercomputing Facility for parallel simulation with COMSOL.

I thank my friends John, Karthik, and Josef for their moral support and helping me with the presentation of this work.

Lastly, I thank Kavya for letting me be as irresponsible a husband I am.

CONTRIBUTORS AND FUNDING SOURCES

This work was sponsored by the Air Force, under SBIR contract FA8650-15-M-2627, (Prime Contractor: Physics, Materials, and Applied Mathematics Research L.L.C.)

TABLE OF CONTENTS

Page

LIST OF FIGURES

1. INTRODUCTION

The prospects of modulating light of a particular frequency, by controlling the propagation direction and confining the optical path to a specified region, offers enormous technological applications. For example, step index optical fiber cables with its ability to confine light into its core have revolutionized the telecommunication industry. Most of these novel optical materials are constructed with periodic structures or patterned surfaces to induce sub-micron scale light reflection and scattering, which then interfere constructively or destructively to create macroscale effects [1]. The focus of this work will be on three such materials namely, photonic crystals (PhC), metallic photonic crystals and metasuface based perfect absorbers.

1.1 Photonic crystals

Photonic crystals are a kind of optical analogues of semiconductor crystals. The idea of photonic crystals (or of photonic band gaps) was proposed in 1987 by two independent researchers; Eli Yablonovitch, then working at *Bell communications research* as a method to reduce the losses occurring due to spontaneous emissions from laser [2], and by Sanjeev John, who was working on photon localization [3]. The former then went on to fabricate photonic crystals by drilling cylindrical cavities on a special glass and showing the formation of a complete photonic band gap. The field of photonic crystals then grew rapidly with the advancements of semiconductor fabrication technology. Today there are photonic crystal wave guides, filters and photonic crystal fibers which are commercially available. Proposed applications in future includes tera-hertz router switches with very low power consumption, all optical transistors and even optical integrated circuits.

Photonic crystals are materials with spatial periodicity in their dielectric func-

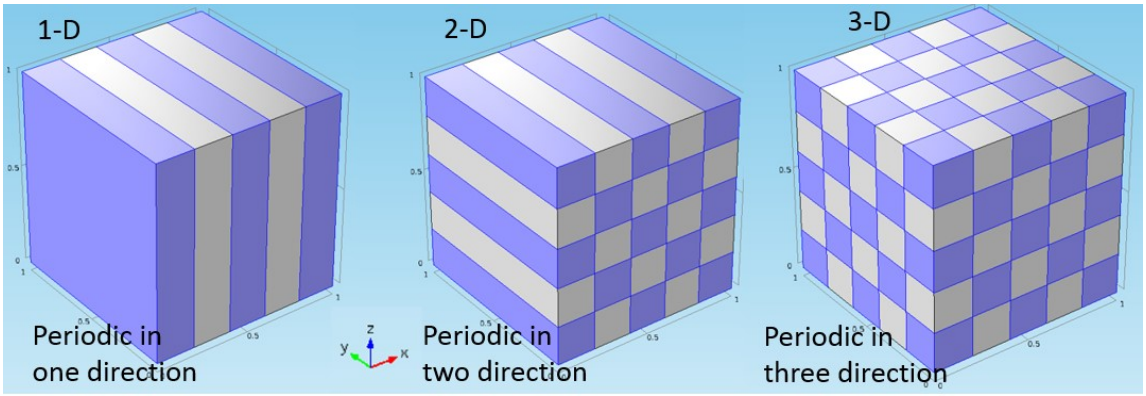

Figure 1.1: A simple illustration of $1, 2$ and 3-dimensional photonic crystals. The two different colors represent two dielectric medium.

tions. This spatial periodicity at sub-wavelength scale of light leads to the formation of photonic band gaps in these materials. Photonic band gaps can be understood as frequency band in which electromagnetic wave propagation are forbidden. Thus, photonic crystals can be used to inhibit the propagation of light in a particular direction or over a certain band of wavelength, while allowing other bands to propagate [4]. The photonic band gaps are similar to electronic band gaps in semiconductors where an electron energy corresponding to the band gap of the semiconductor is forbidden.

The spatial periodicity of the dielectric constant in photonic crystals can be in one, two or three dimensions. A simple illustration of one- two- and three-dimensional photonic crystal is shown in figure 1.1 [1]. The defining feature of the photonic crystal is the periodicity of dielectric material along one or more axes.

Even though photonic crystals can find applications wherever there is a need to manipulate light, fabricating these periodic arrangements are in fact a real challenge. The recent advancement in semiconductor processing can readily be extended to fabricating photonic crystals. One dimensional photonic crystals can be manufactured

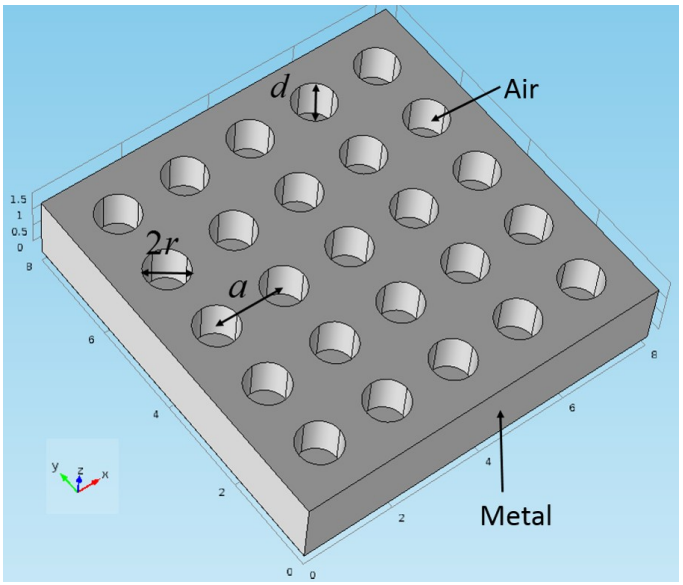

Figure 1.2: A cylindrical cavity two-dimensional photonic crystals consisting of a square array of cylindrical cavities on the surface of metal. d, r are the depth, radius of the cavity respectively and a is the period of square array.

by depositing alternating layers of dielectric materials using chemical vapor deposition (CVD). This is both time consuming as well as requires very precise control of the deposition process. In higher-dimensional photonic crystals, precise positioning of the dielectric medium to prevent scattering losses and high throughput production are still areas of active research [5].

In the first part of this work, the formation of photonic band gaps in one dimensional dielectric photonic crystal will be explained and we review the fabrication methods for one dimensional photonic crystals.

1.2 Cavity type two dimensional metallic photonic crystals

Metallic photonic crystals consists of periodic array of metallic structures. The cavity type metallic photonic crystal (figure 1.2) are made up of two dimensional array of cylindrical cavities on the surface of a metal [6]. Incident light of appropriate

wavelength and wave number couple into propagation modes of the cavity in the surface of the metal which results in strong absorption of specific wavelength at certain angles. The cut-off wavelength is approximately given by the fundamental mode of the cylindrical metallic cavity [7]. This leads to enhanced absorption of radiation shorter the cut off wavelength and strong reflection for wavelength longer than the cut off wavelength. Kirchhoff's law, which states that the directional spectral emissivity must equal the direction spectral absorptivity [8], then implies high emissivity at those selected short wavelengths can be achieved with properly designed metallic photonic crystals.

One of the application of such selective emitter made of two dimensional photonic crystals is illustrated in figure 1.3 [9, 10]. The configuration illustrated known as a thermo photo-voltaic system, forms the mainstay of many solid state thermal to electrical energy conversion devices. The advantage of using two dimensional metallic photonic crystal over a plain emitter is that the photonic crystal can have close to black body emission for a wavelength range suited for the band gap of the photo-voltaic cell. A wide variety of devices using thermo photo-voltaic(TPV) system has been proposed; Solar TPV, Combustion TPV and radioisotope TPV. Two-dimensional metallic photonic crystals made of refractory metals are of great interest since they are more robust and suitable for high temperature application.

Since the refractory metals used for high temperature applications have high density, low machinability and are often expensive, in real applications, metallic photonic crystals are difficult to fabricate and are bulky. A meter square of 1mm thick tantalum will weigh close to 16.4 kg. So any prospect of lowering the weight can further advance the applications of two-dimensional metallic photonic crystals.

In the second section of this thesis, it is proposed to overcome these deficiencies by fabricating a two dimensional metallic photonic crystal using a new method based

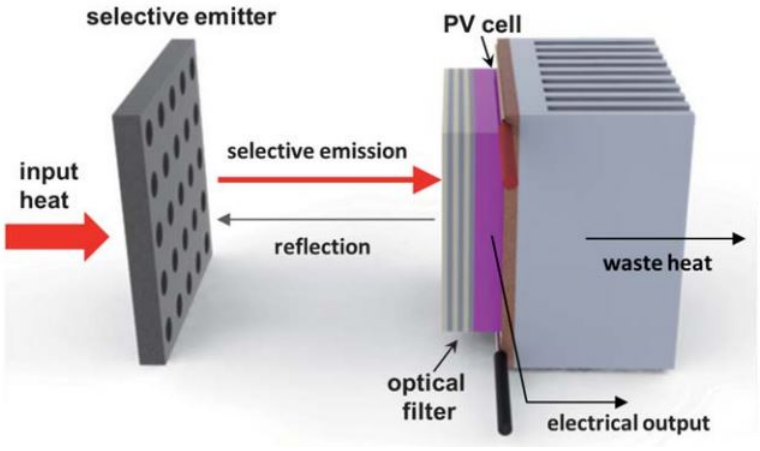

Figure 1.3: An important application of selective emitters are in the field of thermo-photovoltaic energy conversion. The selective emitters made of two dimensional photonic crystals can tailor the emission to suit the band gap of the photo-voltaic (PV) cell. The optical filter only allows photon of energy slightly higher than the band gap of the PV cell to pass through and heat sink helps to maintain the temperature of PV cell.

on depositing a thin film of refractory metal rather than using bulk metal. The optimum design of the metallic photonic crystal providing peak emissivity at a desired wavelength will be arrived at using a full wave simulation of Maxwell's equations

1.3 Metasurface perfect absorbers

Metasurface perfect absorbers on the other hand are recent advances in electromagnetic meta-materials. Metasurfaces usually consists of an array of sub-wavelength scale artificial structures which can have perfect absorption in the microwave, terahertz and infrared region of the electromagnetic spectrum [11]. Perfect absorption of light happen in these structures because they provide impedance matching between the base substrate and the surrounding medium. Metasurface absorbers find applications as photo detectors, sensors, and can also be used in thermo photo-voltaic (TPV) devices where absorption of light is central to the operation.

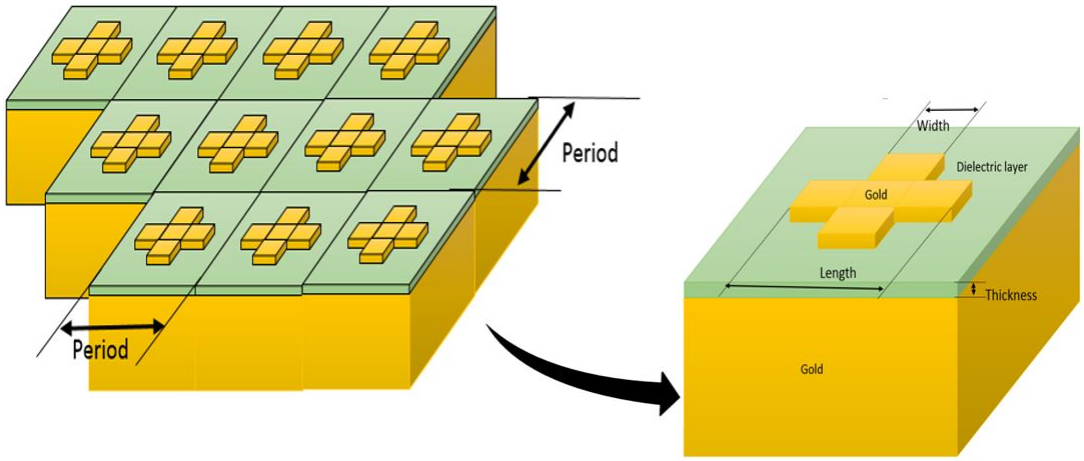

Figure 1.4: An infinite array of cross shaped electric resonators (ER) of gold on top of a thin dielectric layer (in green color). Parameters of an ER unit, namely, thickness of dielectric layer and length of the gold cross that need to be varied to achieve perfect absorption at a desired wavelength.

The first metasurface absorber design which was proposed by Willie J. Padilla *et al.* [12] in 2008 consisted of split wire electric ring resonator design. Later cross shaped design were introduced because of this increased the symmetry of the resonators [13]. The basic construction of cross shaped electric resonator is shown in figure 1.4. A thin layer of dielectric medium (gallium antimonide) is sandwiched between an array of gold crosses on the top and a layer of gold at the base. When light with appropriate wavelength strikes the gold cross-shaped ER, standing electric field with high intensity will be induced in the ER. This in turn causes strong magnetic field resonance in the dielectric layer confined by the top metallic ER and the bottom metal base. These strong electric and magnetic field causes appropriate changes in the dielectric permittivity (ε) and permeability (μ) of the medium which cause the impedance ($\sqrt{\frac{\mu}{\varepsilon}}$) to match that of free space ($\sim 120\pi \ \ \Omega$) for certain wavelength.

This results in complete absorption of these wavelengths.

Compared to one-dimensional and two-dimensional metallic photonic crystals, metasurface based absorbers can provide the following capabilities in controlling the spectral and directional emissivity/absorptivity from a material: 1)Since the ER works by matching the impedance of the medium with that of incident electromagnetic wave, metasurface based absorbers have omni directional absorption capability. 2) By properly selecting the design of the resonator the absorption can be made broadband and polarization independent [14].

Most of the previous studies on the metasurface absorbers focused on wavelength ranges in the mid-infrared $(3 - 8\mu m)$ region of the electromagnetic spectrum. In the last section of the thesis it is proposed to carry out full wave simulations of the Maxwell's equation and to arrive at the design of the cross shaped electric resonator which can provide a peak emission at $2\mu m$. This region known as the shortwave infrared is the preferred spectral region for long-distance telecommunications. The possibility of creating a broadband absorption, at this wavelength region, will also be investigated.

2. ONE DIMENSIONAL PHOTONIC CRYSTAL AND FORMATION OF PHOTONIC BAND GAP

Photonic band gaps are responsible for most of the interesting features associated with a photonic crystal. In this chapter, we present the details regarding the formation of photonic band gaps in one dimensional photonic crystals. Then we review some methods to fabricate one dimensional photonic crystals.

2.1 Formation of photonic band gaps in 1-D photonic crystals

2.1.1 Maxwell's equations

The equations known as 'Maxwell's equations' were presented by James Clarke Maxwell in about 1861. It represents the first 'unification' of two fundamental theories in physics namely the theory of electricity and theory of magnetism, hitherto considered separate, to form the theory of electromagnetism. Maxwell's equation governs all the classical electromagnetic phenomenon especially the propagation of light which we know are electromagnetic waves.

Physical quantities that appear in Maxwell's equation are electric field $\vec{E}$ in V/m, magnetic field $\vec{B}$ in Wb/m^2, electric displacement field $\vec{D}$ in C/m^2, magnetic field intensity $\vec{H}$ in A/m, electric current density $\vec{J}$ in A/m^2, and charge density ρ in C/m^3. These quantities are related using four partial differential equations as presented

below [15]

$$\nabla \times \vec{E} = -\frac{\partial \vec{B}}{\partial t} \tag{2.1}$$

$$\nabla \times \vec{H} = \vec{J} + \frac{\partial \vec{D}}{\partial t} \tag{2.2}$$

$$\nabla . \vec{D} = \rho \tag{2.3}$$

$$\nabla . \vec{B} = 0 \tag{2.4}$$

When studying photonic crystals formed from dielectric materials, we will be dealing with macroscopic regions, without any localized charge or current density, and so we can set the electric current density $\vec{J} = 0$ and the charge density $\rho = 0$ in the above equations. The equations, then consist of eight scalar equations and a total of 12 variables (3 for each of the four vectors $\vec{E}, \vec{H}, \vec{D}$ and $\vec{B}$). To solve this system of equations uniquely, we need to find relationships between $\vec{B}$ and $\vec{H}$ and between $\vec{D}$ and $\vec{E}$.

In response to an applied electric field the medium polarizes and the polarization ($\vec{P}$) is a convolution of the electric field at previous times with time-dependent susceptibility given by $\chi(t)$.

$$\vec{P}(t) = \varepsilon_0 \int_{-\infty}^{+\infty} \chi(t - t')\vec{E}(t')dt' \tag{2.5}$$

The components D_i of the displacement field $\vec{D}$ can be related to the components E_i of the electric field $\vec{E}$ via a power series [16].

$$\frac{D_i}{\varepsilon_0} = \sum_{j=1} \varepsilon_{ij} E_j + \sum_{j,k} \chi_{ijk} E_j E_k + \mathcal{O}(E^3) \tag{2.6}$$

where $\varepsilon_0 \approx \frac{10^{-9}}{36\pi}$ Farad/m is the vacuum permittivity. We could simplify this relation

using the following four arguments/assumption. First, if the field strength (E_i) is small ($\sim 10^3$ V/m) there is a linear relationship between the D_i and E_i, so that χ_{ijk} and all the higher order terms can be neglected. Second, if the material is macroscopic and isotropic then $\vec{E}(\vec{r},\omega)$ and $\vec{D}(\vec{r},\omega)$ are related by ε_0 multiplied by a scalar dielectric function $\varepsilon(\vec{r},\omega)$ also known as the relative permittivity of the material. Third, we assume that there is no frequency dependence of ε and fourth, material is assumed to be transparent so that $\varepsilon(\vec{r})$ is purely real and positive. Similar set of arguments can be put forth for the magnetic field $\vec{B}$ and magnetic field intensity $\vec{H}$ as well, and thus we obtain the constitutive relations,

$$\vec{D}(\vec{r}) = \varepsilon_0\varepsilon(\vec{r})\vec{E}(\vec{r}) \qquad \vec{B}(\vec{r}) = \mu_0\mu(\vec{r})\vec{H}(\vec{r}) \tag{2.7}$$

where $\mu_0 = 4\pi \times 10^{-7}$. For most dielectric materials in the optical frequency range it is safe to assume $\mu(\vec{r}) = 1$ and so $\vec{B}(\vec{r}) = \mu_0\vec{H}(\vec{r})$. In such case, ε (relative permittivity of the material) is the square of the refractive index n of the medium since $n = \sqrt{\varepsilon\mu}$.

Now the Maxwell's equations, with our assumptions, take the form;

$$\nabla \times \vec{E}(\vec{r},t) = -\mu_0\frac{\partial\vec{H}(\vec{r},t)}{\partial t} \tag{2.8}$$

$$\nabla \times \vec{H}(\vec{r},t) = \varepsilon_0\varepsilon(\vec{r})\frac{\partial\vec{E}(\vec{r},t)}{\partial t} \tag{2.9}$$

$$\nabla.[\varepsilon(\vec{r})\vec{E}(\vec{r},t)] = 0 \tag{2.10}$$

$$\nabla.\vec{H}(\vec{r},t) = 0 \tag{2.11}$$

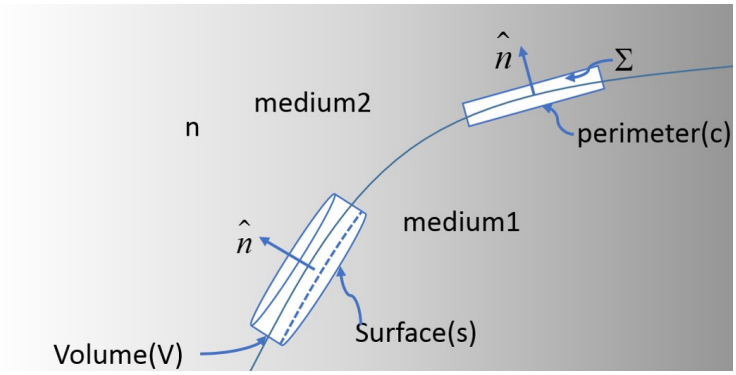

Figure 2.1: A short cylinder at the interface between medium 1 and medium 2. 's' is the surface and 'V' is the volume of the cylinder. A narrow rectangle at the interface between two media. Σ is the area of the rectangle and c is its perimeter

2.1.2 Boundary conditions at interface between macroscopic media

Since our aim is to understand the propagation of electromagnetic waves through a periodically varying dielectric material and to understand the formation of photonic band gap. Therefore, we obtain the relations of the four vectors $\vec{E}, \vec{H}, \vec{D}$ and $\vec{B}$ across an interface separating two dielectric materials.

Consider a squat Gaussian pill pox that straddles the interface between the medium 1 and medium 2 as shown in figure 2.1. The end cap of the cylinder are parallel to the surface of the interface. If we integrate the two divergence equation (2.3, 2.4) of the Maxwell's equation over the surface area of this pillbox and using the Gauss divergence theorem,

$$\int_V \nabla.\vec{F} dV = \oint_S \vec{F}.d\vec{s},. \tag{2.12}$$

The surface integral reduces in the limit as the height of the cylinder approaches zero to an integral over the end caps only and gives a relation for the magnetic field and

electric displacement field across the interface as:

$$\vec{n}.(\vec{B}_2 - \vec{B}_1) = 0,\ \vec{n}.(\vec{D}_2 - \vec{D}_1) = \sigma, \tag{2.13}$$

where σ is the surface charge density in $\mathrm{C/m^2}$ and $\vec{n}$ is the normal directed from medium 1 to 2. This is equivalent to saying that the normal component of the magnetic induction $\vec{B}$ is continuous across the interface and the difference in the normal component of the electric displacement fields, $\vec{D}$, is equal in magnitude to the surface charge density σ.

Now, consider a rectangular loop formed by two infinitesimally separated parallel line element one located in medium 1 and other in medium 2 as shown in figure 2.1. If we integrate the curl equations ((2.1,2.2)) over the area bound by this rectangle and apply the Stokes theorem

$$\int_{\Sigma} (\nabla \times \vec{F}).d\vec{s} = \oint_{C} \vec{F}.d\vec{l} \tag{2.14}$$

to both the sides of the curl equations (2.1,2.2), we see that the contour integral in the limit as the width of the rectangle approaches zero. This gives the relation between the electric field and magnetic field intensity between the two media as:

$$\vec{n} \times (\vec{E}_2 - \vec{E}_1) = 0,\ \vec{n} \times (\vec{H}_2 - \vec{H}_1) = \vec{K}, \tag{2.15}$$

where again $\vec{n}$ is the normal defined previously from medium 1 to medium 2 and $\vec{K}$ is the surface current density in A/m. In other words, this says that the tangential component of the electric field vector $\vec{E}$ is continuous across the interface and the difference between the tangential component of the magnetic field intensity $\vec{H}$ is equal to the surface current density $\vec{K}$. All the situations considered in this thesis

will pertain to the case where we have $\sigma = 0$ and $\vec{K} = 0$. Then, we have the continuity of the tangential component of the magnetic field intensity $\vec{H}$ and the normal component of the electric displacement $\vec{D}$ as well. These relations will play an important part in our analysis of the layered media or 1D photonic crystals.

2.1.3 Wave equation and monochromatic plane wave

In this section, we use the Maxwell's equation to obtain the wave equation. A simple solution to the wave equation is the plane wave solution. Further on, we study some of the characteristics of a plane wave. Substituting equation (2.7) for the $\vec{B}$ in the first of the Maxwell's equation and applying a curl operation gives us:

$$\nabla \times \vec{E} = -\frac{\partial \vec{H}}{\partial t} \tag{2.16}$$

$$\nabla \times \left(\frac{1}{\mu}\nabla \times \vec{E}\right) = -\frac{\partial}{\partial t}\nabla \times \vec{B} \tag{2.17}$$

$$\nabla \times \left(\frac{1}{\mu}\nabla \times \vec{E}\right) = -\varepsilon\frac{\partial^2 \vec{E}}{\partial t^2} \tag{2.18}$$

Using two vector identities, (i) Curl of a scalar times a vector is equal to the scalar times curl of the vector plus gradient of scalar curl vector, and (ii) the curl of curl of a vector is equal to the gradient of divergence of the vector minus the laplacian of

the vector. We see

$$\nabla \times \left(\frac{1}{\mu}\nabla \times \vec{E}\right) = \frac{1}{\mu}\nabla \times (\nabla \times \vec{E}) + \left(\nabla \frac{1}{\mu}\right) \times (\nabla \times \vec{E}) \quad (2.19)$$

$$\nabla \times (\nabla \times \vec{E}) = \nabla(\nabla.\vec{E}) - \nabla^2 \vec{E} \quad (2.20)$$

$$\nabla^2 \vec{E} - \nabla(\nabla.\vec{E}) = \mu\varepsilon \frac{\partial^2 \vec{E}}{\partial t^2} - (\nabla \ln \mu) \times (\nabla \times \vec{E}) \quad (2.21)$$

$$\nabla.\vec{D} = 0 \quad (2.22)$$

$$\varepsilon \nabla.\vec{E} = -\vec{E}.\nabla\varepsilon + \nabla.(\varepsilon \vec{E}) \quad (2.23)$$

$$\nabla^2 \vec{E} - \nabla(\vec{E}.\nabla \ln \varepsilon) = \mu\varepsilon \frac{\partial^2 \vec{E}}{\partial t^2} - (\nabla \ln \mu) \times (\nabla \times \vec{E}) \quad (2.24)$$

which is the wave equation for the vector field $\vec{E}$. In a homogeneous isotropic medium the gradient of the logarithm of ε and μ equal to zero and the equation reduces to a more familiar form of the Helmholtz equation:

$$\nabla^2 \vec{E} - \mu\varepsilon \frac{\partial^2 \vec{E}}{\partial t^2} = 0 \quad (2.25)$$

$$\nabla^2 \vec{H} - \mu\varepsilon \frac{\partial^2 \vec{H}}{\partial t^2} = 0 \quad (2.26)$$

The solutions to the above equation are monochromatic plane waves:

$$\vec{E} = \vec{E}_0 e^{i(\omega t - \vec{k}.\vec{r})} \vec{H} = \vec{H}_0 e^{i(\omega t - \vec{k}.\vec{r})} \quad (2.27)$$

Substituting this solution back in the equation we can see that the wave vector $\vec{k}$ and the angular frequency ω are related to μ, ε as $|\vec{k}| = \omega\sqrt{\mu\varepsilon} = \omega n$, where n is the refractive index of the medium.

The plane wave is a function of both time and space. At some instant of time (t), $\omega t - \vec{k}.\vec{r} = constant$ represents the equation of a plane. Such electromagnetic waves are called plane waves and the wave fronts (a surface containing points affected in the

same way by a wave at time t) are planar. Differentiating $\omega t - \vec{k}.\vec{r} = constant$ with respect to time, we see that the surfaces of constant phase travel in the direction of $\vec{k}$ with a phase velocity $v = \omega/k$. The wavelength of such a wave is $\lambda = 2\pi/k = 2\pi v/\omega$. The phase velocity can also be expressed as $1/\sqrt{\mu\epsilon}$. In vacuum, the phase velocity $c = 1/\sqrt{\mu_0\varepsilon_0} = 2.99 \times 10^8 m/s$ and the refractive index of a medium is given by $n = c/v = \sqrt{\mu_r\varepsilon_r}$. The ε_r is a function of the frequency and therefore the refractive index of the material is also a function of frequency. The variation of the refractive index with frequency gives rise to the well-known phenomenon of dispersion.

The vector $\vec{E}_0$ and $\vec{H}_0$ in equation (2.27) can be written as $\vec{E}_0 = \hat{u}_1 E_0$ and $\vec{H}_0 = \hat{u}_2 H_0$, where u_1 and u_2 are the two unit vectors representing the polarization of the wave. H_0 and E_0 are the complex amplitudes that are constant in space and time. Substituting these in the divergence equation (2.3, 2.4) tells us that $\hat{u}_1.\vec{k} = \hat{u}_2.\vec{k} = 0$. i.e the $\vec{E}$ and $\vec{H}$ are perpendicular to the direction of propagation given by $\vec{k}$. Thus the electromagnetic waves are transverse waves. Substituting $\vec{E}_0 = \hat{u}_1 E_0$ and $\vec{H}_0 = \hat{u}_2 H_0$ into the curl equation gives us another restriction on the field vectors:

$$\hat{u}_2 = \frac{\vec{k} \times \hat{u}_1}{|\vec{k}|} \tag{2.28}$$

Therefore, $\hat{u}_1$, $\hat{u}_1$ and $\vec{k}$ form a triad of perpendicular vectors. The amplitude electric field and magnetic field of a wave can be related as $H_0 = E_0/\eta$, where $\eta = \sqrt{\mu/\varepsilon}$ is called the impedance of the medium. Using Poynting's theorem, the average flux of energy carried by this plane wave is given by:

$$\langle \vec{S} \rangle = \frac{1}{2} Re[\vec{E} \times \vec{H}^*] = \frac{|E_0|^2 \hat{k}}{2\eta} = \frac{\vec{k}|E_0|^2}{2\omega\mu} \tag{2.29}$$

and the time averaged energy density is given by

$$\langle U \rangle = \frac{1}{2}\varepsilon |E_0|^2 \tag{2.30}$$

We note that the energy flux is directed in the direction of propagation and energy flux is equal to the phase velocity times the energy density.

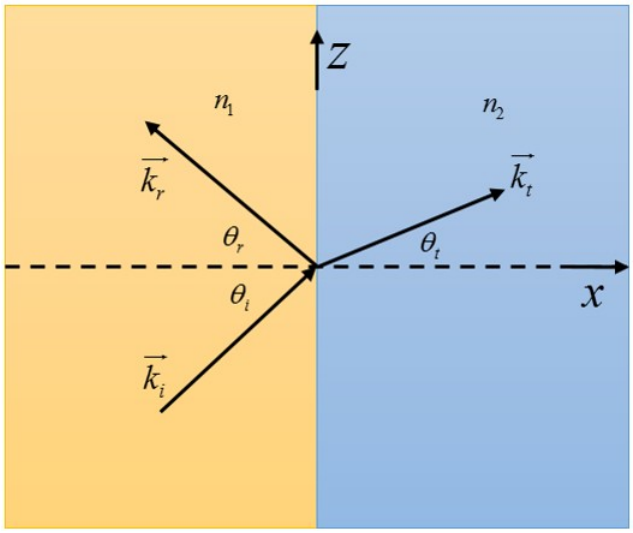

Figure 2.2: A plane wave is incident ($\vec{k}_i$) at the interface between two media giving rise to a reflected ($\vec{k}_r$) and transmitted light ($\vec{k}_t$).

2.1.4 Reflection and refraction of monochromatic waves at the boundary

The Maxwell's equation and the boundary conditions for the electric and magnetic fields across the interface of materials, lets us observe what happens when a plane monochromatic wave is incident on the interface between two media. In general, an electromagnetic wave incident on a layer could either be reflected, absorbed, transmitted, scattered or could generate surface electromagnetic waves. We assume

that: the material is non-absorbing, the incident wave frequency is highly offset from the plasma resonance frequency of the material, and the surface is perfectly smooth to prevent any scattering. Then the major effects on the incident plane wave are the reflection back to first medium and the transmission to the second medium.

Let the incident plane wave be denoted by $\vec{E}_i e^{[i(\omega t - \vec{k}_i.\vec{r}]}$ and because of the linearity of the Maxwell's equation, the reflected and transmitted waves are also plane waves and can be denoted by $\vec{E}_r e^{[i(\omega t - \vec{k}_r.\vec{r}]}$ and $\vec{E}_t e^{[i(\omega t - \vec{k}_t.\vec{r}]}$, respectively. Here ω represents the angular frequency of the incident wave and $\vec{k}_i$, $\vec{k}_r$ and $\vec{k}_t$ are the propagation vectors of the incident reflected and transmitted waves, respectively (see figure 2.2). The boundary conditions (discussed in section 2.1.2) have to hold independent of any particular time. Therefore, at all times at x=0, for any boundary condition relating the amplitudes to exist, the exponential terms should match. i.e $(\vec{k}_i.\vec{r})_{x=0}$=$(\vec{k}_r.\vec{r})_{x=0}$=$(\vec{k}_t.\vec{r})_{x=0}$. This is the mathematical equivalence of the statement– the incident wave the reflected wave and the transmitted wave at the interface all lie in a same plane, known as the plane of incidence.

We also note that the boundary condition should hold for any value of z at the interface $x = 0$. This is only possible if the exponential terms are equal, i.e the phases of the incident wave, the reflected wave and transmitted wave matches along the interface. For the fields to match at the boundary the phase velocity along the interface $x = 0$ (along z) should be the same, $(\vec{k}_i)_{alongz}$=$(\vec{k}_r)_{alongz}$=$(\vec{k}_t)_{alongz}$ which implies $|\vec{k}_i| \sin\theta_i$=$|\vec{k}_r| \sin\theta_r$=$|\vec{k}_t| \sin\theta_t$ and since $|\vec{k}_k| = \omega n_k/c$ we have

$$n_1 \sin\theta_i = n_1 \sin\theta_r = n_2 \sin\theta_t \tag{2.31}$$

which is the Snell's law.

The polarization state (the direction of $\hat{u}_1$ and how it behaves at particular lo-

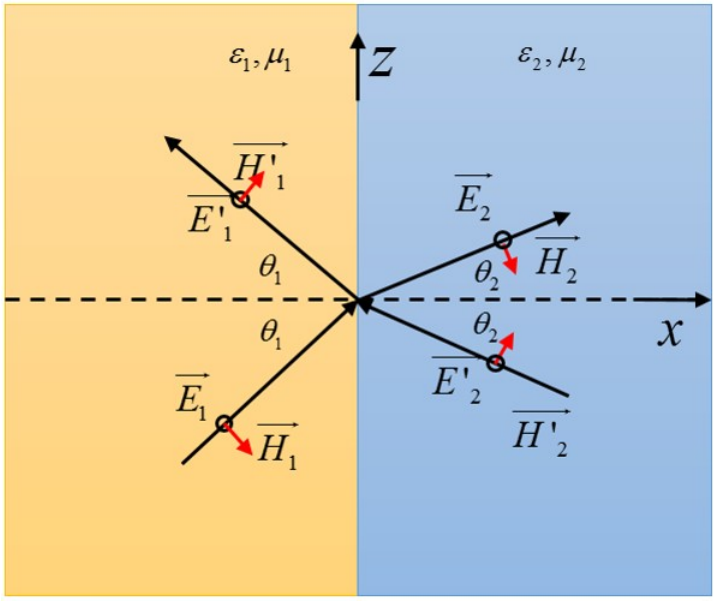

Figure 2.3: A plane **s**-polarized wave is incident at the interface between two dielectric media. The primes indicate right propagating waves.

cation over time) of the wave becomes important when dealing with reflection and refraction at an interface. For the first part consider **s**-polarized or plane polarized light with electric field oscillation perpendicular to the plane of incidence. A similar wave is shown in figure 2.3. The two media are designated 1 and 2, respectively. Because of the linearity of the wave equation, the general solution of the wave equation can be taken as the superposition of the incident and reflected wave (or a left propagating and right propagating wave) in each medium.

$$\vec{E} = \begin{cases} (\vec{E}_1 e^{-i\vec{k}_1.\vec{r}} + \vec{E'}_1 e^{-i\vec{k'}_1.\vec{r}}) e^{i\omega t} & x < 0 \\ (\vec{E}_2 e^{-i\vec{k}_2.\vec{r}} + \vec{E'}_2 e^{-i\vec{k'}_2.\vec{r}}) e^{i\omega t} & x > 0 \end{cases} \tag{2.32}$$

The primes indicate right propagating part. From equation 2.15, the tangential component of the $\vec{E}$ field and the tangential component of the $\vec{H}$ should be conserved

across the interface:

$$E_{1s} + E'_{1s} = E_{2s} + E'_{2s} \tag{2.33}$$

$$\sqrt{\frac{\varepsilon_1}{\mu_1}}(E_{1s} - E'_{1s})\cos\theta_1 = \sqrt{\frac{\varepsilon_2}{\mu_2}}(E_{2s} - E'_{2s})\cos\theta_2 \tag{2.34}$$

where the subscript 's' denotes an **s**-polarized wave. This equation can be written in matrix form as:

$$D_s(1)\begin{pmatrix} E_{1s} \\ E'_{1s} \end{pmatrix} = D_s(2)\begin{pmatrix} E_{2s} \\ E'_{2s} \end{pmatrix} \tag{2.35}$$

where $D_s(i)$ the dynamical matrix for **s**-polarized wave is

$$D_s(i) = \begin{pmatrix} 1 & 1 \\ \sqrt{\frac{\varepsilon_1}{\mu_1}}\cos\theta_i & -\sqrt{\frac{\varepsilon_1}{\mu_1}}\cos\theta_i \end{pmatrix} \tag{2.36}$$

The reflection coefficient (r) is defined as the ratio of the reflected electric field amplitude to the incident electric field amplitude and transmission coefficient (t) is defined as the ratio of the transmitted electric field amplitude to the incident electric field amplitude.

$$r_s = \left(\frac{E'_{1s}}{E_{1s}}\right)_{E'_{2s}=0} = \frac{n_1\cos\theta_1 - n_2\cos\theta_2}{n_1\cos\theta_1 + n_2\cos\theta_2} \tag{2.37}$$

$$t_s = \left(\frac{E'_{2s}}{E_{1s}}\right)_{E'_{2s}=0} = \frac{2n_1\cos\theta_1}{n_1\cos\theta_1 + n_2\cos\theta_2} \tag{2.38}$$

Similarly, the **p**-polarized wave the magnetic field is perpendicular to the incident plane. The continuity of the tangential component of the $\vec{E}$ field and the tangential

component of the $\vec{H}$ implies:

$$(E_{1p} + E'_{1p})\cos\theta_1 = (E_{2p} + E'_{2p})\cos\theta_2 \tag{2.39}$$

$$\sqrt{\frac{\varepsilon_1}{\mu_1}}(E_{1p} - E'_{1p}) = \sqrt{\frac{\varepsilon_2}{\mu_2}}(E_{2p} - E'_{2p}) \tag{2.40}$$

The primes indicate the right propagating part and the subscript p reminds that the wave is **p**-polarized. Therefore, the last two equations can be written in matrix form as:

$$D_p(1)\begin{pmatrix} E_{1p} \\ E'_{1p} \end{pmatrix} = D_p(2)\begin{pmatrix} E_{2p} \\ E'_{2p} \end{pmatrix} \tag{2.41}$$

where the dynamical matrix for the **p**-polarized

$$D_p(i) = \begin{pmatrix} \cos\theta_i & \cos\theta_i \\ \sqrt{\frac{\varepsilon_i}{\mu_i}} & -\sqrt{\frac{\varepsilon_i}{\mu_i}} \end{pmatrix} \tag{2.42}$$

Finally, the reflection (r) and transmission coefficients (t) are given by:

$$r_p = \left(\frac{E'_{1s}}{E_{1s}}\right)_{E'_{2s}=0} = \frac{n_1\cos\theta_1 - n_2\cos\theta_2}{n_1\cos\theta_1 + n_2\cos\theta_2} \tag{2.43}$$

$$t_p = \left(\frac{E'_{2s}}{E_{1s}}\right)_{E'_{2s}=0} = \frac{2n_1\cos\theta_1}{n_1\cos\theta_1 + n_2\cos\theta_2} \tag{2.44}$$

which is the Fresnel relation.

2.1.4.1 Thin film between two semi-infinite media

Using the matrix approach developed in the last section, consider a homogeneous medium of thickness d sandwiched between two semi-infinite media as shown in figure 2.4. A plane wave is incident on the medium from the left, and because of the continuous translational symmetry along the z-direction the solution to Maxwell's

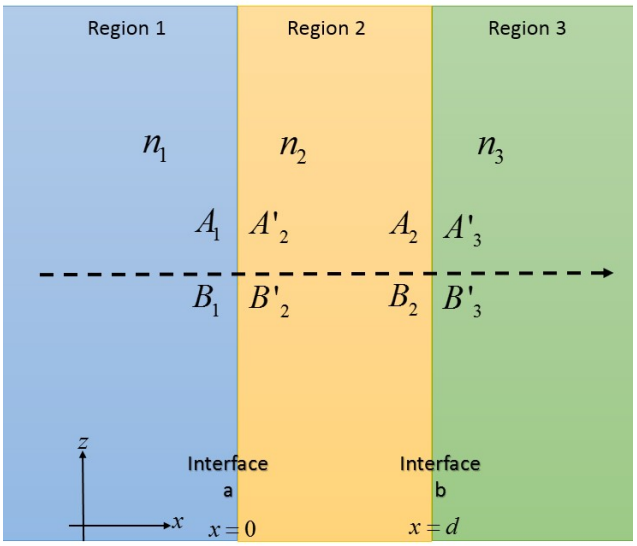

Figure 2.4: A homogeneous medium of thickness d and refractive index n_2 sandwiched between two semi infinite media of refractive index n_1 and n_3

equation can be assumed to be of the form:

$$\vec{E} = E(x)e^{i(\omega t - \beta z)} \tag{2.45}$$

where β is the component of the wave vector along the z direction. Because of the multiple reflection and transmission at two interfaces the variation of the x-component of the electric field can be considered to be the sum of a left propagating and right propagating waves in each of the three regions as shown below:

$$E(x) = Re^{-ik_x x} + Le^{ik_x x} = A(x) + B(x) \tag{2.46}$$

where A(x) represents the amplitude of the right propagating wave and B(x) represents that of the left propagating wave. Across the interface a, as shown in figure 2.4, we may relate the amplitude of the right and left propagating waves as seen

previously as:

$$D(1)\begin{pmatrix} A_1 \\ B_1 \end{pmatrix} = D(2)\begin{pmatrix} A_2' \\ B_2' \end{pmatrix} \tag{2.47}$$

or

$$\begin{pmatrix} A_1 \\ B_1 \end{pmatrix} = D^{-1}(1)D(2)\begin{pmatrix} A_2' \\ B_2' \end{pmatrix} = D_{12}\begin{pmatrix} A_2' \\ B_2' \end{pmatrix} \tag{2.48}$$

Similarly, for the interface b D(2):

$$\begin{pmatrix} A_2 \\ B_2 \end{pmatrix} = D_{23}\begin{pmatrix} A_3' \\ B_3' \end{pmatrix} \tag{2.49}$$

where $D(i)$ is the dynamic matrix as defined separately for **s** and **p** polarized wave by (2.36, 2.42). Within a medium (region 2) separated by d in the x-direction we can relate the phase change occurring between the left end and right end as:

$$\begin{pmatrix} A_2' \\ B_2' \end{pmatrix} = P_2\begin{pmatrix} A_2 \\ B_2 \end{pmatrix} = \begin{pmatrix} e^{i\phi_2} & 1 \\ 1 & e^{-i\phi_2} \end{pmatrix}\begin{pmatrix} A_2 \\ B_2 \end{pmatrix} \tag{2.50}$$

assuming that the wave is propagating only in the xz-plane and the wave vector makes an angle θ with the normal to the interface. Then the z-component of the wave vector is given by: $\beta = n_j \frac{\omega}{c}\sin\theta_j$ and the x-component is given by: $k_{jx} = n_j \frac{\omega}{c}\cos\theta_j$ so $\phi_2 = k_{2x}d$ where index j denotes respective region. From 2.47, 2.48, 2.50, we see that

$$\begin{pmatrix} A_1 \\ B_1 \end{pmatrix} = D_{12}P_2D_{23}\begin{pmatrix} A_3' \\ B_3' \end{pmatrix} \tag{2.51}$$

This method mentioned above can be extended to any number of layers.

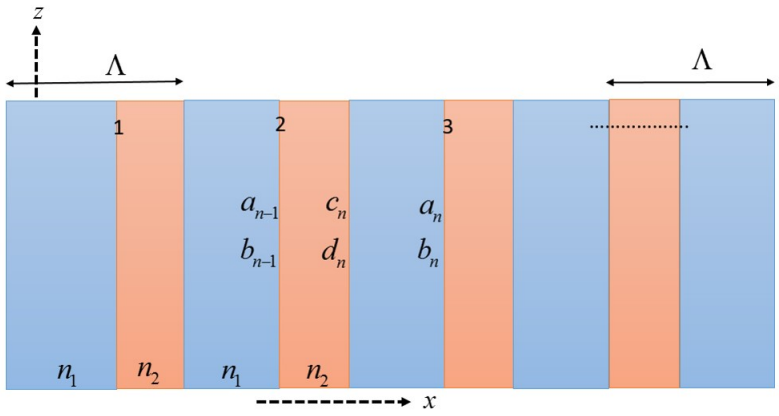

Figure 2.5: A periodic multilayer of periodicity Λ and refractive index n_1 and n_2

.

2.1.5 Periodic layered media

In a periodic media, the index of refraction varies with the layers in a periodic pattern. So there exists a symmetry element in these structures that the whole system is invariant under translation by an integer multiple of the distance Λ, known as the period, in a particular direction (as shown in figure 2.5). Referring to the figure, the index of refraction varies along the x-direction and can be given by:

$$n(x) = \begin{cases} n_2, & 0 < x < l_2 \\ n_1, & l_1 < x < \Lambda \end{cases} \tag{2.52}$$

and $n(x) = n(x + \Lambda)$ and $l_1 + l_2 = \Lambda$ where l_1 and l_2 are the thickness of the two repeating media, respectively. As discussed in the preceding section, we may write the electric field as:

$$\vec{E} = E(x)e^{i(\omega t - \beta z)} \tag{2.53}$$

where β is the z-component of the wave vector (continuous translational symmetry along the z-direction). The x-component of the electric field in nth unit cell can be written as the sum of the left propagating and right propagating waves within each medium as:

$$E(x) = \begin{cases} a_n e^{-ik_{1x}(x-n\Lambda)} + b_n e^{ik_{1x}(x-n\Lambda)}, & n\Lambda - a < x < n\Lambda \\ c_n e^{-ik_{2x}(x-n\Lambda+a)} + d_n e^{ik_{2x}(x-n\Lambda+a)}, & (n-1)\Lambda - a < x < n\Lambda - a \end{cases} \tag{2.54}$$

However,

$$k_{jx} = \left[\left(\frac{n_j \omega}{c} \right)^2 - \beta^2 \right]^{1/2} = \frac{n_j \omega}{c} \cos\theta_j \tag{2.55}$$

From the relations discussed in the previous section:

$$\begin{pmatrix} a_{n-1} \\ b_{n-1} \end{pmatrix} = D_{12} P_2 \begin{pmatrix} c_n \\ d_n \end{pmatrix} \tag{2.56}$$

and

$$\begin{pmatrix} c_n \\ d_n \end{pmatrix} = D_{21} P_1 \begin{pmatrix} a_n \\ b_n \end{pmatrix} \tag{2.57}$$

where

$$P_j = \begin{pmatrix} e^{i\phi_j} & 1 \\ 1 & e^{-i\phi_j} \end{pmatrix} \tag{2.58}$$

, $\phi_j = k_{1x} a$ in the first medium, and $\phi_j = k_{2x} b$ in the second medium. We can

evaluate $D_{12}P_2$ for an **s**-polarized wave as:

$$
\begin{aligned}
D_{12}P_2 &= \begin{pmatrix} 1 & 1 \\ n_1\cos\theta_1 & -n_1\cos\theta_1 \end{pmatrix}^{-1} \begin{pmatrix} 1 & 1 \\ n_2\cos\theta_2 & -n_2\cos\theta_2 \end{pmatrix} \begin{pmatrix} e^{ik_{2x}b} & 1 \\ 1 & e^{-ik_{2x}b} \end{pmatrix} \\
&= \begin{pmatrix} e^{ik_{2x}b}\left(1+\frac{n_2\cos\theta_2}{n_1\cos\theta_1}\right) & e^{-ik_{2x}b}\left(1-\frac{n_2\cos\theta_2}{n_1\cos\theta_1}\right) \\ e^{ik_{2x}b}\left(1-\frac{n_2\cos\theta_2}{n_1\cos\theta_1}\right) & e^{-ik_{2x}b}\left(1+\frac{n_2\cos\theta_2}{n_1\cos\theta_1}\right) \end{pmatrix} \qquad (2.59) \\
&= \begin{pmatrix} e^{ik_{2x}b}\left(1+\frac{k_{2x}}{k_{1x}}\right) & e^{-ik_{2x}b}\left(1-\frac{k_{2x}}{k_{1x}}\right) \\ e^{ik_{2x}b}\left(1-\frac{k_{2x}}{k_{1x}}\right) & e^{-ik_{2x}b}\left(1+\frac{k_{2x}}{k_{1x}}\right) \end{pmatrix} \qquad (2.60)
\end{aligned}
$$

where we use the relation 2.55 to get the last equation. When we substitute 2.57 in 2.56, we get:

$$
\begin{pmatrix} a_{n-1} \\ b_{n-1} \end{pmatrix} = D_{12}P_2D_{21}P_1 \begin{pmatrix} a_n \\ b_n \end{pmatrix} \qquad (2.61)
$$

2.1.5.1 Bloch Waves and Band structure

The behavior of waves in a periodic structure is governed by the Bloch-Floquet theorem which states that the allowable modes ($\vec{E}(x)$ in our case) in the case of a periodic media is given by the product of periodic function and wave. Therefore, the solution of the wave equation for the periodic case should be of the form:

$$
\vec{E}_W(x,z) = E_W(x)e^{i\beta z}e^{-iWx} \qquad (2.62)
$$

where $E_W(x)$ is the periodic function with a period Λ that is $E_W(x+\Lambda) = E_W(x)$ and e^{-iWx} denotes the wave part. The function, $E_W(x)$, depends on W, where W is known as the Bloch wave number. In terms of the matrix representation this can be

written as:

$$\begin{pmatrix} a_n \\ b_n \end{pmatrix} = e^{iW\Lambda} \begin{pmatrix} a_{n-1} \\ b_{n-1} \end{pmatrix} \tag{2.63}$$

This further means that the Bloch wave should satisfy the following eigenvalue problem:

$$D_{12}P_2D_{21}P_1 \begin{pmatrix} a_n \\ b_n \end{pmatrix} = \begin{pmatrix} A & B \\ C & D \end{pmatrix} \begin{pmatrix} a_n \\ b_n \end{pmatrix} = e^{iW\Lambda} \begin{pmatrix} a_n \\ b_n \end{pmatrix} \tag{2.64}$$

Therefore, the factor $e^{iW\Lambda}$ is the eigenvalue of the translation matrix and since the determinant of the translational matrix is equal to 1 (why?), $AD - BC = 1$. We can see that

$$e^{iW\Lambda} = 1/2(A + D) \pm \sqrt{[1/2(A + D)]^2 - 1} \tag{2.65}$$

and the corresponding eigenvectors are given by:

$$\begin{pmatrix} a_n \\ b_n \end{pmatrix} = \begin{pmatrix} B \\ e^{iW\Lambda} - A \end{pmatrix} \tag{2.66}$$

Since $e^{-iW\Lambda}$ should also be an eigenvalue of the matrix and equating the real part from Eq. 2.65, we have the allowable Bloch wave numbers:

$$\cos(W\Lambda) = (A + D)/2 \tag{2.67}$$

$$W(\beta, \omega) = \frac{1}{\Lambda} \cos^{-1}[(A + D)/2] \tag{2.68}$$

Notice that for the W to be real, the absolute value of half the trace of the matrix in 2.64 i.e. $|(A + D)/2|$ should be less than or equal to 1. These correspond to the waves that are allowed to propagate in the medium. However, when $|(A + D)/2| > 1$, W becomes complex and from 2.62 the allowed mode will have an exponentially

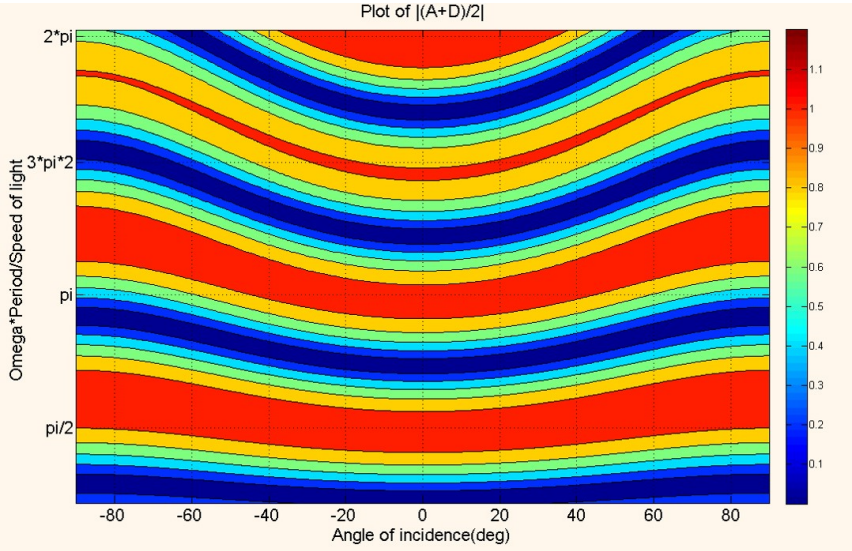

Figure 2.6: A plot of the band gaps. Region shown in red color with the value of $|(A+D)/2| > 1$ corresponds to evanescent waves.

decreasing factor. Such waves are known as evanescent waves. A plot of the allowable W as a function of the frequency ω normalized by c/Λ and various angles of incidence is shown in figure 2.6. The dispersion relation between W and ω at normal incidence, corresponding to $\beta = 0$, is shown in figure 2.7.

If we have N unit cells of periodic layered medium, each with two layers of thickness a and b, we can extend 2.61 and 2.64 to obtain:

$$\begin{pmatrix} a_0 \\ b_0 \end{pmatrix} = \begin{pmatrix} A & B \\ C & D \end{pmatrix}^N \begin{pmatrix} a_N \\ b_N \end{pmatrix} \tag{2.69}$$

now the N^{th} power of the matrix can be simplified using the following relation:

$$\begin{pmatrix} A & B \\ C & D \end{pmatrix}^N = \begin{pmatrix} AU_{N-1} - U_{N-2} & BU_{N-1} \\ CU_{N-1} & DU_{N-1} - U_{N-2} \end{pmatrix} \tag{2.70}$$

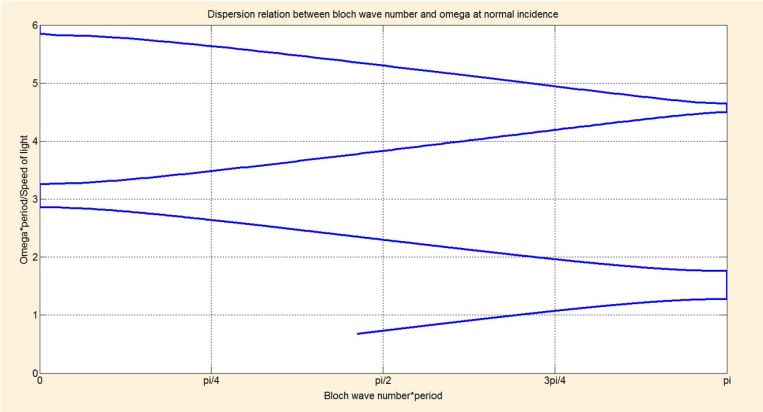

Figure 2.7: Dispersion relation for a photonic crystal when the angle of incidence is 90°, and the refractive index of the media 1 and 2 are 1.5 and 2.62, respectively. Thelength of each layer = 129 nm=$\Lambda/2$

where $U_N = \frac{\sin(N-1)W\Lambda}{\sin(W\Lambda)}$. Using this simplification and the reflection coefficient for such a medium is defined as:

$$r_N \equiv \left(\frac{b_0}{a_0}\right)_{b_N=0} = \frac{CU_{N-1}}{AU_{N-1} - U_{N-2}} \tag{2.71}$$

Now the ratio of the reflected power to the incident power defined as the reflectance of this N unit cell layer can be calculated using the Poynting's power flow equation:

$$\langle \vec{S} \rangle = \frac{\vec{k}|E_0|^2}{2\omega\mu} \tag{2.72}$$

So the reflectance (R) (ratio of the reflected power to incident power) can be calculated by taking the absolute square of r_N:

$$R = |r_N|^2 = \frac{|C|^2}{|C|^2 + \left(\frac{\sin(W\Lambda)}{\sin(NW\Lambda)}\right)^2}$$

A plot of reflectance for such a medium with 50 unit cells consisting of refractive

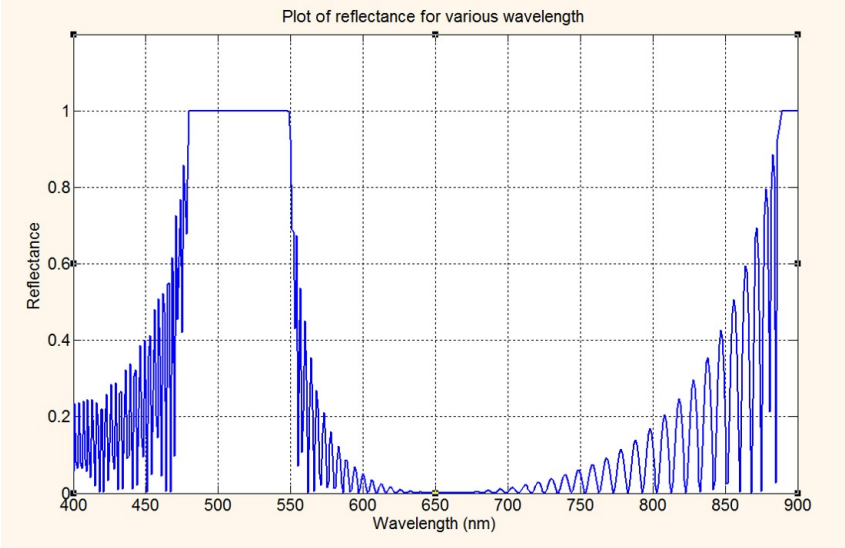

Figure 2.8: A plot of reflectance for such a medium with 50 unit cells consisting of refractive indices 1.5 and 2.62 are shown. The band gap at around 500 nm.

indices 1.5 and 2.62 are shown in Figure 2.8. The band gap at around 100 nm. We can clearly see the band gap at around 500 nm.

2.2 Review of current fabrication methods for 1-D photonic crystals

As seen in the last section, one dimensional photonic crystals are constructed out of multiple layers of alternating high and low refractive index materials. Conventional method to fabricate such structure includes film growth techniques like molecular beam epitaxy (MBE), pulsed laser deposition (PLD), chemical vapor deposition (CVD), RF sputtering and thermal evaporation. However, most of these methods are either expensive, time consuming or controlling the precise layer thickness is difficult. In order to overcome these drawbacks, current methods to fabricate one dimensional photonic crystal use methods based on spin coating, photolithography or electron beam lithography, and microfabrication etching techniques such as plasma etching, focused ion beam and chemical etching. A review of these new techniques to fabricate photonic crystals are presented below.

Spin coating: The component material is first dissolved in a suitable solvent and is applied on to a substrate. The substrate is then rotated at high speed so that the centrifugal force spreads the component material, dissolved in the solvent, uniformly over the substrate. The solvent then evaporates partly while spinning and partly during the subsequent heating step. There are two factors that must be considered when using the spin coating method to fabricate one dimensional photonic crystals of alternating dielectric. First, both the substrate and the solvents should have sufficient adhesive force to enable them to be spin coated on each other. The second factor is that the solvent of one should not dissolve the other component material. The spin coating method can be extended to fabricate organic [17] or organic and inorganic hybrid [18] one dimensional photonic crystal.

Sol gel method is another simple and inexpensive method for the fabrication of thin films. In this technique, a gel solution is formed by hydrolysis and poly-

condensation reaction of an organometallic precursor (typically metal alkaloids and metal chlorides) in water (sol). This gel solution can then be spin coated on to a substrate. After spin coating, the substrate is heated and dried to evaporate the remaining solvent to leave a porous layer on the substrate. This method is typically suited for the fabrication of oxides of silicon and titanium [19]. The procedure can be easily extended to achieve a large area and the layer thickness can be controlled by adjusting the spin coating parameters such as spin speed, duration of the spin and the concentration of the precursor during the gel formation. This technique allows fine control of the final chemical composition. Even small quantities of dopants like organic dyes and other rare earth elements can also be introduced into the sol.

Electrochemical micro-machining method was presented by Billaro [20] in 2002. The electrochemical micro-machining method combines photolithography and electrochemical etching. The general fabrication process of the electrochemical micro-machining is illustrated in Figure 2.9. A 100 nm thick SiO_2 layer is deposited on the surface of an n-doped (100) oriented silicon wafer.Periodic patterns are created on top of the SiO_2 layer using photolithography. Chemical etching using buffered HF can be used to remove the exposed SiO_2 layer and KOH isotropically etches the silicon underneath. Then the electrochemical micromachining of silicon using hydrofluoric acid as electrolyte [21] is adopted to obtain the photonic crystal. This method is good for the fabrication of large scale one dimensional photonic crystals.

Interfernce lithography (holographic lithography): The periodic intensity variation created by the interference of multiple laser beams can be used to fabricate periodic dielectric microstructures [22]. A variable phase retardation mask is used to control the laser beams so as to control the width and spacing of the interference

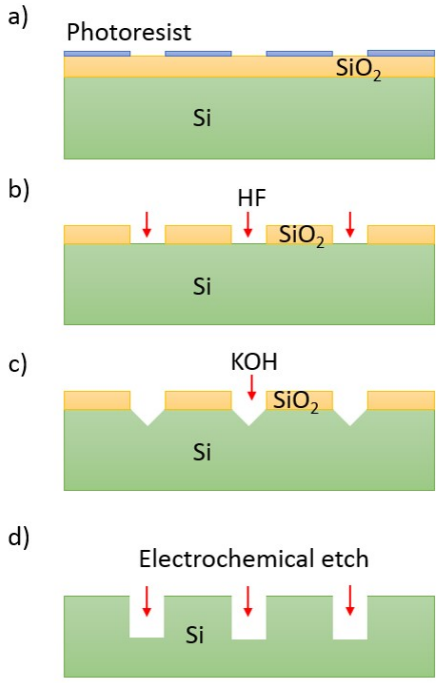

Figure 2.9: Various processes in the fabrication of one dimensional photonic crystal using electrochemical etching. a) Pattern definition by photolithography, b) Removal of the exposed SiO_2 using HF. c) Isotropic etching of Si using KOH and d) Electrochemical etching of Si using HF as electrolyte.

pattern. The intensity distribution of the interference pattern can be given by

$$I(\vec{r},t) = \langle \sum_{i}^{n} \vec{E}_i^2 \rangle + \sum_{i<j}^{n} 2\vec{E}_i\vec{E}_j \cos[(\vec{k}_i - \vec{k}_j).\vec{r} + (\phi_i - \phi_j)] \tag{2.73}$$

where i and j represent different laser beams, $\vec{E}_i$ and ϕ_i are the electric field and the initial phase and $\vec{k}_i$ is the wave vector. The interference pattern can be controlled by changing the polarization and the magnitude of the electric field, the direction of the wave vector, and the phase of the incident laser beams. Thus it is possible to fabricate various one dimensional periodic patterns when the photoresist is exposed by interference patterns. This is followed by etching of the exposed region to obtain

the one dimensional photonic crystals.

3. METALLIC 2-D PHOTONIC CRYSTALS

In this chapter, we look at two dimensional metallic photonic crystals. From a theoretical point of view, we attempt to understand how by varying a few geometrical parameters we can control the emissivity from the surface. This will be followed by extensive simulations to arrive at a standard methodology to calculate the optimal design of photonic crystals providing peak emissivity/absorptivity at a required wavelength. Further in the chapter, we review some standard methods to fabricate two dimensional photonic crystals and then we fabricate thin layer two dimensional tantalum photonic crystals.

3.1 Theory of metallic 2-D photonic crystals

Two dimensional photonic crystals have periodic variation of the dielectric constants along two perpendicular directions and is homogeneous in the third direction. Here we will be dealing with a special kind of two dimensional (2D) photonic crystals know as metallic photonic crystals where the design consists of a square array of cylindrical cavities on the surface of a metal. Metallic photonic crystals are distinct because they can be designed to have near blackbody emittance at a given wavelength range while having very low emittance at other wavelengths. One of many applications of such a selective emitter is in thermo-photovoltaic energy conversion. For example, a refractive metal which could withstand very high temperature, with an array of cylindrical cavities, could be used as a source radiating most of its energy in the infrared region onto a photo voltaic cell with band gap in the infrared region.

A two dimensional metallic photonic crystal is shown in Figure 3.1. This design provides emissivity close to one at shorter wavelengths and low emittance at longer wavelength. This enhancement of the emissivity at shorter wavelengths can be un-

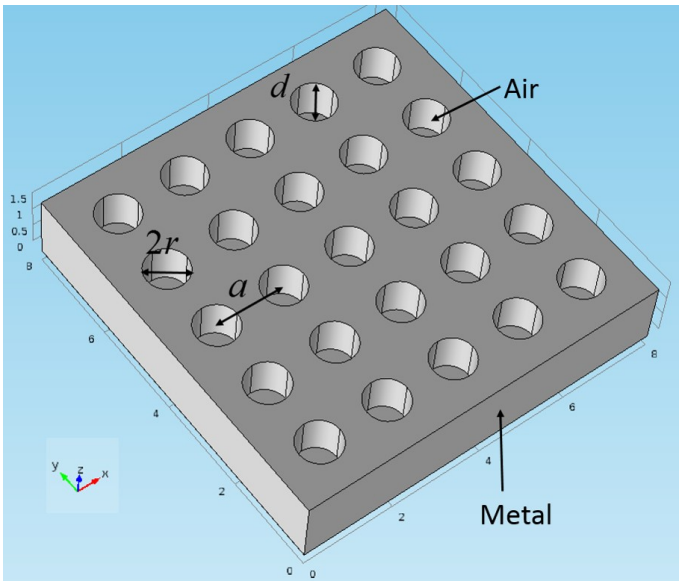

Figure 3.1: A two dimensional metallic photonic crystal: A square array of cylindrical cavities on a plain metal surface. The radius and depth of each cylinder is r and d. The square array has a period a.

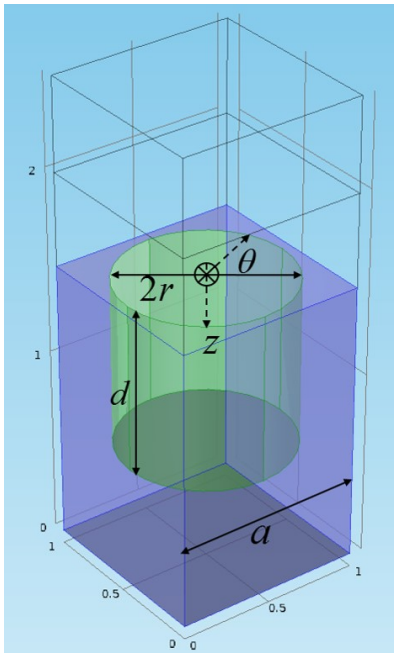

Figure 3.2: A unit cell of the two dimensional metallic photonic crystal. The cylindrical polar coordinate system is also shown where positive z-axis indicates the depth.

derstood in terms of the coupling of incident plane electromagnetic radiation into resonant cavity electromagnetic modes in the cylindrical holes on the metal surface. First, the field above the photonic crystal unit cell is expanded as a plane wave basis. Second, the field inside the holes is expanded as a linear combination of waveguide modes then by comparing the modes the coupling can be understood. This can be best explained using rigorous coupled-mode theory [23, 24].

Imagining a plane wave interacting with one unit cell of the metallic photonic crystal where the unit cell, shown in Figure 3.2, consists of a cylindrical air cavity on a plane metal surface. The electric field of the incident plane wave can be expanded in Fourier space onto plane wave basis as shown below. For any wave that is traveling in the direction $\vec{\beta}$ the Bloch-Floquent periodicity gives:

$$\vec{E}(\vec{r}) = e^{-j\vec{\beta}.\vec{r}} \sum_{n=-\infty}^{\infty} \sum_{m=-\infty}^{\infty} \sum_{p=-\infty}^{\infty} \vec{S}(m,n,p).e^{j(\frac{2\pi m}{\Lambda_1}+\frac{2\pi n}{\Lambda_2}+\frac{2\pi p}{\Lambda_3}).\vec{r}} \tag{3.1}$$

$$= \sum_{n=-\infty}^{\infty} \sum_{m=-\infty}^{\infty} \sum_{p=-\infty}^{\infty} \vec{S}(m,n,p).e^{-j(\vec{\beta}-\frac{2\pi m}{\Lambda_1}-\frac{2\pi n}{\Lambda_2}-\frac{2\pi p}{\Lambda_3}).\vec{r}} \tag{3.2}$$

$$= \sum_{n=-\infty}^{\infty} \sum_{m=-\infty}^{\infty} \sum_{p=-\infty}^{\infty} \vec{S}(m,n,p).e^{-j\vec{k}(m,n,p).\vec{r}} \tag{3.3}$$

where Λ_i is the period in the i-th direction. For our system with periodicity in the x and y-direction we can write

$$E_i(x,y,z) = e^{-jk_z z} \sum_{n=-\infty}^{\infty} \sum_{m=-\infty}^{\infty} S_i(m,n).e^{-j[k_x(m)x+k_y(n)y]} \tag{3.4}$$

where $k_x(m) = \beta_x - \frac{2\pi m}{\Lambda_x}$ and $k_y(n) = \beta_y - \frac{2\pi n}{\Lambda_y}$. Of these plane wave modes that are incident on the metal surface, some modes are able to couple into the cavity. Similar to the periodic layered media of the last chapter some modes are forbidden inside the cylindrical air cavity. Now let us identify the modes that are allowed inside the cavity

that is open on one side. The modes allowed inside such a cavity can be estimated by assuming it as a both end closed, perfectly conducting, cylindrical cavity of same radius but of twice the depth. We note that the eigenmodes of the closed cavity is the same as an open cavity with mirroring boundary condition at the top. The cavity modes can be classified broadly as transverse electric (TE) and transverse magnetic (TM).

We can now calculate the allowable modes in a cylindrical cavity with perfectly conducting walls. The electric field inside the cylinder is governed by the Helmholtz equation and we simplify the analysis by using the cylindrical polar coordinate illustrated in Figure 3.2

$$\nabla^2 \vec{E} = \frac{1}{c^2} \frac{\partial^2 \vec{E}}{\partial t^2} \tag{3.5}$$

For transverse magnetic (TM) field distribution, the z component of the electric field, E_z, follows the scalar Helmholtz equation [25]:

$$\frac{\partial^2 E_z}{\partial r^2} + \frac{1}{r}\frac{\partial E_z}{\partial r} + \frac{1}{r^2}\frac{\partial^2 E_z}{\partial \theta^2} + \frac{\partial^2 E_z}{\partial z^2} = \frac{1}{c^2}\frac{\partial^2 E_z}{\partial t^2} \tag{3.6}$$

If we now assume a solution of the form $E_z(r, \theta, z, t) = E(r)e^{jn\theta}e^{j(-k_z z - \omega t)}$ and substitute this back in 3.6 and perform variable separation to obtain the differential equation:

$$\frac{d^2 E_z}{dr^2} + \frac{1}{r}\frac{dE_z}{dr} + \left(\frac{\omega^2}{c^2} - \frac{n^2}{r^2} - k_z^2\right) E_z = 0 \tag{3.7}$$

$$r^2\frac{d^2 E_z}{dr^2} + r\frac{dE_z}{dr} + \left[r^2\left(\frac{\omega^2}{c^2} - k_z^2\right) - n^2\right] E_z = 0 \tag{3.8}$$

The solutions to this differential equation are the Bessel functions where the depen-

dence of the fields on the azimuthal angle (with 2π period) requires that n should be an integer.

Then, E_z can be given as $E_z(z,\theta,r,t) = E_0 J_n(k_{nm}r)e^{jn\theta}e^{j(-k_z z-\omega t)}$ where J_n is the $n-$th order Bessel function. In transverse magnetic (TM) fields, where B_z should be zero, the boundary condition require that E_z needs to be zero for any θ and z, at r=R. This implies that $k_{nm} = \zeta_{nm}/R$ where ζ_{nm} denotes the $m-$th zero of the $n-$th Bessel function. This represents one restriction on the electric field mode along the radial direction.

In the z-direction if the flat conducting ends of the cavity are at *z=2d* and *z=0*, we have the normal component of the electric field to be zero at *z=2d* and *z=0*. This means $\sin k_z 2d = 0$ and $k_z d = l\pi$ where l is an integer. Then the allowable modes in the metal cavity corresponds the frequency:

$$\omega_{nml} = c\sqrt{\left(\frac{\zeta_{nm}}{R}\right)^2 + \left(\frac{\pi l}{2d}\right)^2} \tag{3.9}$$

Similar analysis can be carried out for the transverse electric (TE) mode where $B_z(r,\theta,z,t) = B_0 J_n(k_{nm}r)e^{in\theta}e^{-j(k_z z+\omega t)}$. The boundary conditions (ref section 2.1.2) lead us that $\partial B_z/\partial r = 0$ at $r = R$ which means $k_{nm} = \xi_{nm}/R$, where ξ_{nm} is the $m-$th maxima or minima of the $n-$th order Bessel function. Therefore, the allowable modes in the air cylindrical cavity can be given by:

$$\omega_{nml} = c\sqrt{\left(\frac{\xi_{nm}}{R}\right)^2 + \left(\frac{\pi l}{2d}\right)^2} \tag{3.10}$$

In summary, there is a frequency below which there are no field distributions that can be permitted inside the cavity. There is also a corresponding cutoff wavelength λ_c. So the incident modes below the cutoff frequency will not transmit any energy

into the cavity. Below the cutoff frequency, the incident radiation will not sense the cavity and most of the incident radiation is reflected off as if from a plain metal. If the metal with in the cavity were perfectly absorbing, then all the energy that is transmitted inside by the coupled modes would have been completely absorbed by the metal.

Two dimensional metallic photonic crystals are also influenced by the surface propagation modes [26, 27, 28]. The plane incident waves could induce surface charge oscillations and thus longitudinal modes that propagate along the metal surface are generated in addition to the cavity modes. These modes, however, are confined within the air metal interface and now the cavity mode energy reduces as part of the incident energy is coupled to the surface modes. The dispersion relation for the surface wave is given by:

$$|\vec{k}_{sp}| = \frac{\omega}{c}\left(\frac{\varepsilon_r}{\varepsilon_r + 1}\right)^{1/2} \tag{3.11}$$

where ω is the frequency of the surface wave and ε_r is the real part of the dielectric function of the metal. The surface waves are generated due to the periodicity parallel to the interface and the longitudinal wave vector ($\vec{k}_{\|}$) magnitudes are increased by the reciprocal lattice vector $\vec{T}$ of the periodic grating as $\vec{k}_{\|} + n\vec{T} = \vec{k}_{sp}$ (as shown in figure 3.3). Then the surface wave modes can be given by the relation:

$$\left(\frac{\varepsilon_r}{\varepsilon_r + 1}\right) = \left(\sin\theta\cos\phi + n\frac{2\pi c}{\omega\Lambda_x}\right)^2 + \left(\sin\theta\sin\phi + m\frac{2\pi c}{\omega\Lambda_y}\right)^2 \tag{3.12}$$

For surface modes, when the electrons are oscillating there is damping and gradually some part of the energy is absorbed and some part is reemitted because of the oscillation of electron. Now, the absorption or reemission from the metal will depend on the damping coefficient of the metal [29].

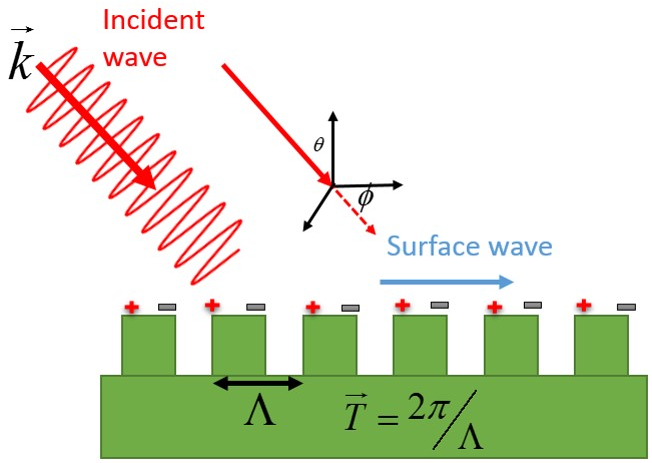

Figure 3.3: Surface waves are generated due to the periodicity and the longitudinal wave vector magnitudes are increased by the reciprocal lattice vector of the periodic grating is $\vec{k}_{\parallel} + n\vec{T} = \vec{k}_{sp}$

The cavity modes were derived assuming that the tangential electric field at the metal interface is zero. This is valid if the metal is a perfect conductor of infinite conductance (σ). However, in reality, the conductance (σ) is finite and this causes a finite surface current density (J) in the Maxwell's equation. This translates that the refractive index of the metal will consist of an imaginary part which is responsible for the rapid attenuation of the electric field within the metal. The attenuation occurs within a region known as the skin depth of the metal. The skin depth of the metal is a function of the frequency and is approximately few micrometers (1- 5 μm) in the GHz range. This imaginary component of the refractive index is responsible for the absorption of electromagnetic waves by the metal.

Once inside the cylinder, some amount of the radiation is absorbed with each reflection inside the cylinder as the metal is lossy (shows finite conductance). This leads to the absorption of some amount of energy, with each reflection, that had been coupled into the cavity modes. Part of the radiation escapes back (i.e. towards

the incident direction) from the cavity after multiple reflections. Now the escaped radiation along with the reflected radiation from the surface could interfere and this then, enhances or reduces the net reflection from the surface.

From the Kirchhoffs law of thermal radiation, the directional spectral absorption should equal the directional spectral emission. Therefore, perfect absorbers at a particular wavelengths are also perfect emitters at that wavelength and vice versa. So, the metallic photonic crystal with near unity absorptivity at shorter wavelengths will have high emissivity at those wavelengths.

Consider a photonic crystal design with a square array of period, $a = 1000$ nm on a tungsten surface with cylinders of radius $r = 450$ nm and depth $d = 560$ nm. For such a cavity, the frequency of the lowest allowable mode of the cavity is given by TE_{111}. The TE_{111} mode predicts that from Eq. 3.10, $\omega_{111}=1.5\times10^{15}$ rad/s which corresponds to a wavelength of 1270 nm. Figure 3.4 shows the calculated emissivity for the same tungsten photonic crystal from a full wave simulation of the Maxwell's equation in the unit cell domain. From the simulation the max peak emission corresponds to 1310 nm.

The deviation from the prediction is expected as we assumed that the walls of the metal cavity are perfectly conducting while deriving Eq. 3.10. A second reason for the deviation from our theoretical study is that the modes may not be simple TM and TE modes as we assumed.

What would happen if instead of a tungsten photonic crystal a tantalum or any other metal was used? The answer is that as predicted from the modes inside the cylinder we will still have peak emissivity at around 1270nm however the absorptivity need not be anywhere close to that of a black body (as shown in Figure 3.4). The reason for this being that the intrinsic absorptivity of the metals vary with frequency. If the metal is having a good intrinsic absorptivity at the wavelength corresponding

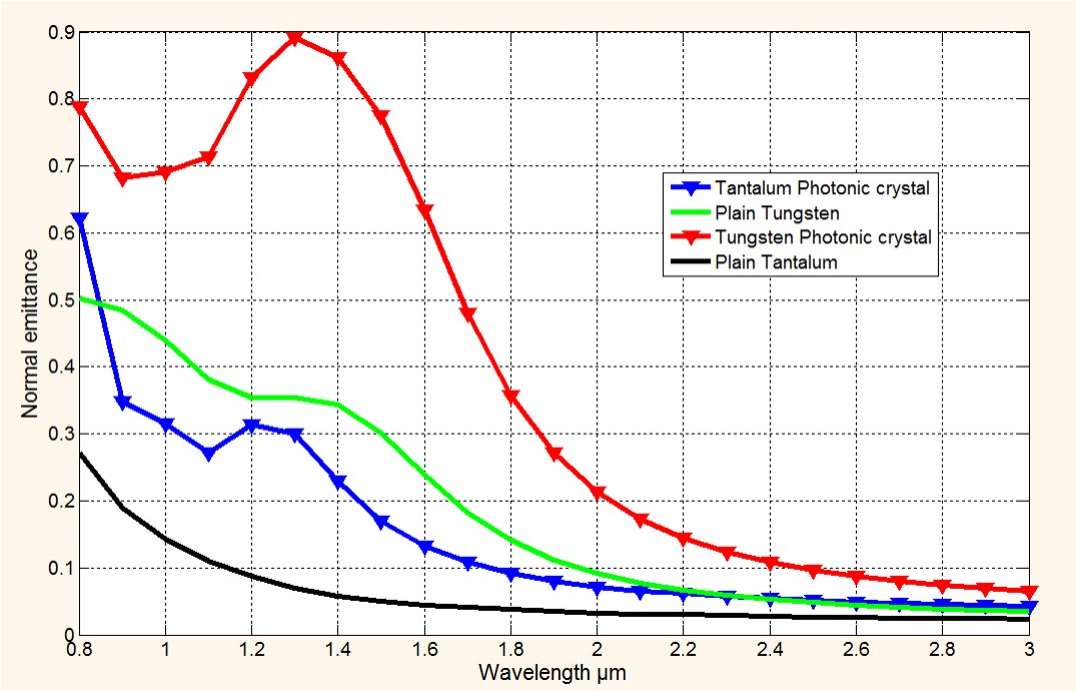

Figure 3.4: Simulated spectral emissivity plot of a tungsten photonic crystal with radius r=450nm, depth d=560nm and period a=1000nm is shown in red color. Spectral emissivity from a tungsten photonic crystal with the same dimensions is shown in blue. Green shows the intrinsic emissivity of tungsten.

to the one that is allowed inside the cylinder we will have an added effect and we can realize near unity aborption. A more elaborate description of the above concept is provided in reference [7].

We now have three design parameters in designing a 2D metallic photonic crystals: radius, depth of the cylinder, and the choice of the metal. For a given depth d, increasing the radius decreases the fundamental frequency mode and increases the corresponding cutoff wavelength (λ_c). Even though increasing the depth for a constant radius increases the number of reflections within the cavity and the probability of absorption, there lies an optimum depth, d, for each radius.

The effect of varying the depth of the cavity is plotted in the Figure 3.1. As the

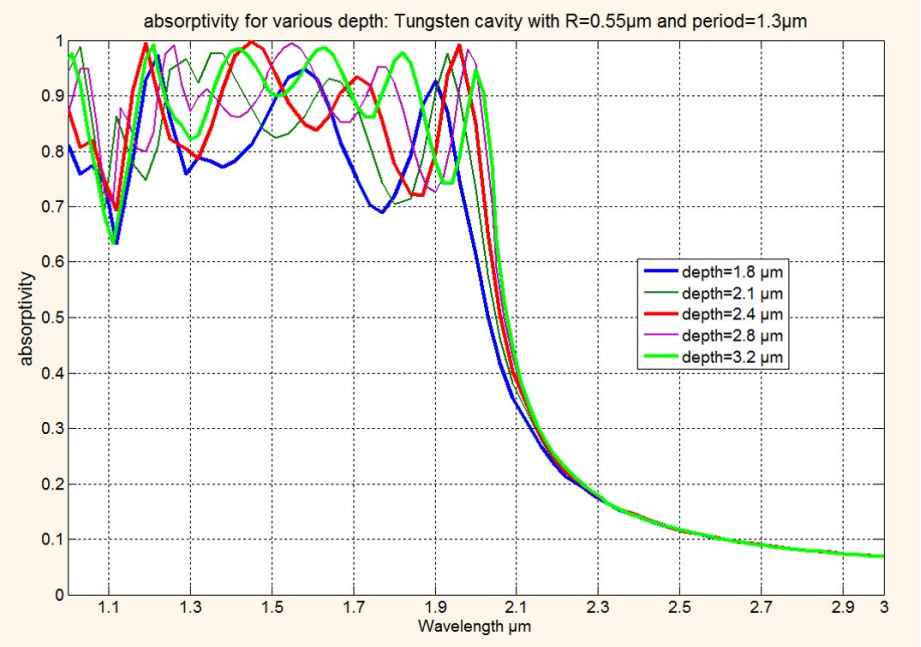

Figure 3.5: Simulated normal spectral absorptivity plot of a tungsten photonic crystal with radius r=550nm, period a=1300nm and varying depth d=1800nm, 2100nm, 2400nm, 2800nm and 3200nm is shown.

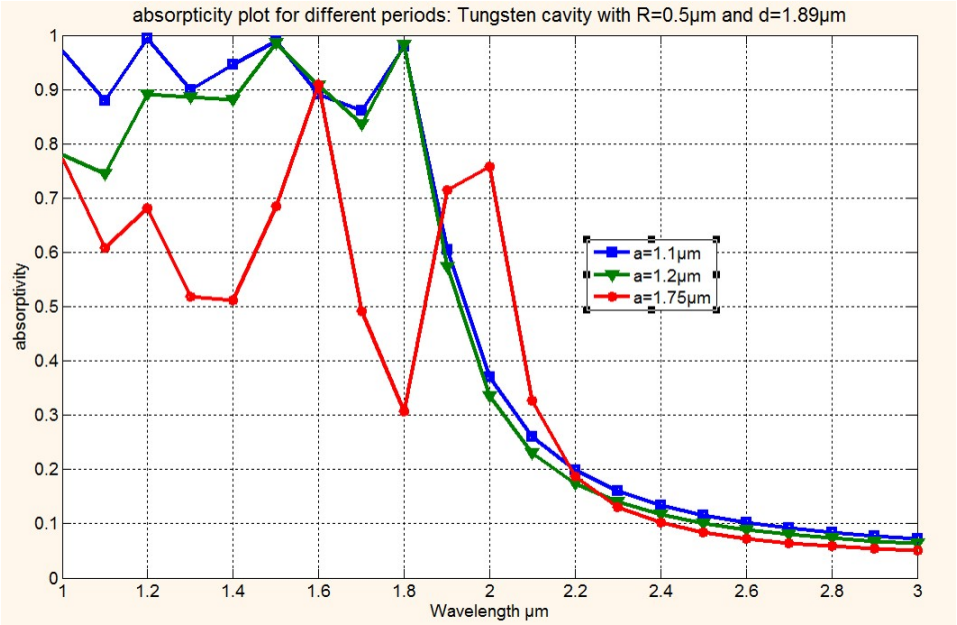

Figure 3.6: Simulated normal spectral absorptivity plot of a tungsten photonic crystal with radius r=500nm, depth d=1890nm and varying periods a=1100nm, 1200nm and 1750nm is shown.

depth increases (in 1 μm to 2 μm range) the area under the normal spectral absorptivity curve increases. However, we notice that there exists an optimum d value from the peaks of various depths around 2 μm. The optimum peak (corresponding to a depth of 2.4 μm), shown in Figure 3.1 as a red line, only has the maximum absorptivity around 2 μm. As we move away from this value the peak emissivity starts to decrease. So even though the total absorption across the spectrum increases monotonically if we want to have a unity absorption spectrum at a specified wavelength we cannot increase the depth indefinitly. This is because at the optimum depth we have a destructive interference of the light coming out and the light that is reflected off the surface, which was the reason for our increase absorbtion.

Finally, we assess the effect of the fourth design parameter namely the period of the cylindrical cavities. A plot of absorption spectrum for three a values is shown in Figure 3.6. As a decreases the percentage of the cavities on the flat surface increases and so there is better absorption. At longer periods, with the onset of diffraction light starts escaping from the surface at different angle and this leads to lower absorptivity at higher periods.

In summary the absorptivity is mainly determined by three things: 1) The efficiency of the coupling between free space propagation modes and eigenmodes inside the cavity. 2) Suitable choice of the metal so that the light that is coupled in to the cavity is abosorbed by the cavity walls. 3) Preventing the escaping of light from the cavity (Ensuring that the reflected lights destructively interfere) by suitable choice of the depth and keeping the period below the onset of diffraction.

3.2 Simulation of 2-D metallic photonic crystal

3.2.1 Simulation of 2-D bulk Ta photonic crystal at 3.5 μm

The discussion of the previous section provided us with many guidelines for designing a 2D metallic photonic crystal-based selective emitter. However, to arrive precisely at the optimum design of the photonic crystal, providing the peak absorption/emission at a selected wavelength, we choose to solve the Maxwell's equation using a finite element scheme and simulate what happens when a plane wave is incident on the surface of the photonic crystal. The metal surface consisting of an infinite array of cylindrical cavities can be simulated by considering just one unit cell with periodic boundary conditions along the lateral direction. This unit cell is illustrated in Figure 3.7. A plane wave polarized in the x-direction travels from the boundary 1 (in air) to the tantalum surface with cylindrical cavity of depth *d*, diameter *2r*, and period *a*. Periodic boundary conditions are imposed on planes perpendicular to x and y-axes to replicate the two dimensional periodicity. For simulation purposes, we used tantalum metal whose optical properties are obtained from [30]. A perfectly scattering boundary condition is assumed at the bottom of the simulation domain. We aim to maximize at a the absorptivity at a wavelength of 3.5μm. This wavelenght correspond to the blackbody emisssion peak of a body at a temperature of 800 K. A period of 200nm was chosen because that is around the minimum feature size that can be fabricated by using an optical lithography system using 355nm UV light.

Solving the Maxwell's equation using full wave simulation, the reflectance of the photonic crystal can be calculated using the net power flow along z-direction through a plane immediately above the surface of the metal. From the reflectance we can obtain the absorptance using the relation $\alpha + \rho = 1$. and then from the Kirchoff's relation, we can obtain the emissivity. In this study, the required diameter and depth

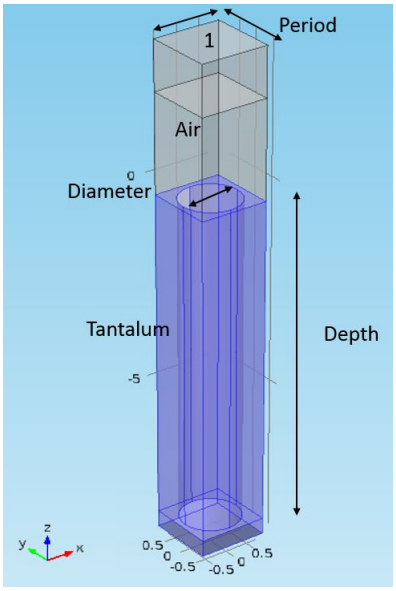

Figure 3.7: The simulation domain of the two dimensional metallic photonic crystal. A plane electromagnetic wave is incident on the tantalum surface with cylindrical cavity (shown in blue) from the port 1. The cavity has a depth 'd', diameter '$2r$' and period 'a' in the x and y direction.

of tantalum cylindrical cavity photonic crystal to obtain emissivity ~ 1 at wavelength close to 3.5μm will be identified. Figure 3.8 shows the emissivity results obtained for six wavelengths (from 3.0μm to 5.5μm) using a batch numerical simulation done using COMSOL Multiphysics by varying the diameter a and the depth d of the cylindrical cavity of the tantalum photonic crystal. The diameter was varied from 1.5μm to 3.4μm and the depth was varied from 10.5μm to 20μm . More than 8000 parameter combinations have been simulated in the batch simulation analysis.

Figure 3.9 shows the method used to determined the optimum diameter $2r$ and the depth d for cylindrical cavity of two dimensional tantalum photonic crystal. The optimum value are $2r = 2.10\mu$m and $d = 16.0\mu$m to provide near unity thermal emissivity at $\lambda = 3.5\mu$m. The plot of spectral emissivity of this tantalum photonic crystal with $2r = 2.10\mu$m and $d = 16.0\mu$m is illustrated in Figure 3.10

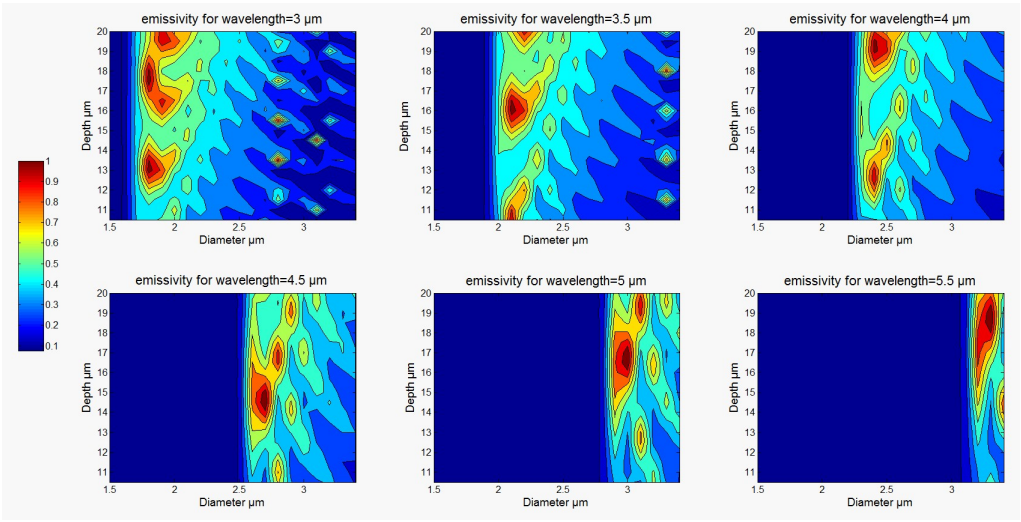

Figure 3.8: Contour plot of the thermal emissivity of tantalum photonic crystal as a function of the diameter and depth of the cylindrical cavities at wavelengths from 3.0μm to 5.5μm.

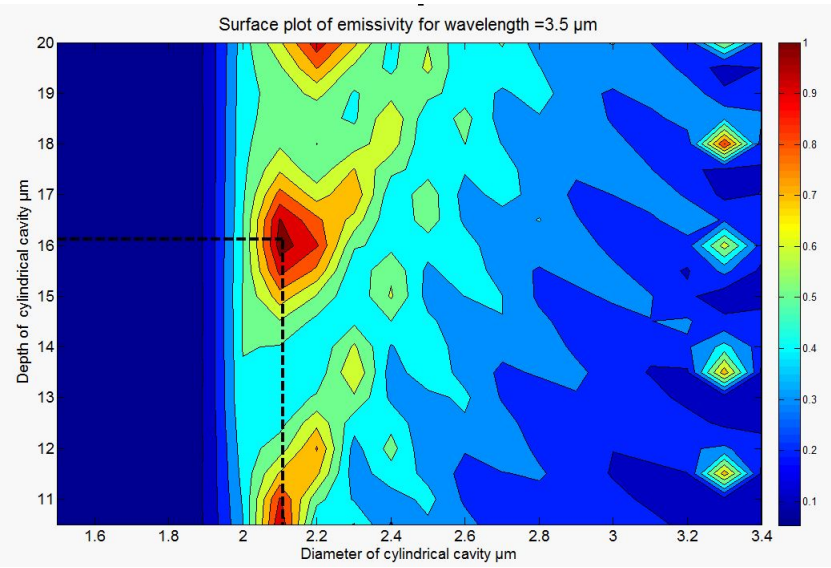

Figure 3.9: Illustration of the method to determine the optimized diameter *2r* and depth d of the cylindrical cavities of the tantalum photonic crystal to provide near unity thermal emissivity at $\lambda = 3.5\mu$m. The optimum values are $2r = 2.10\mu$m and $d = 16.0\mu$m. see dependence on r.

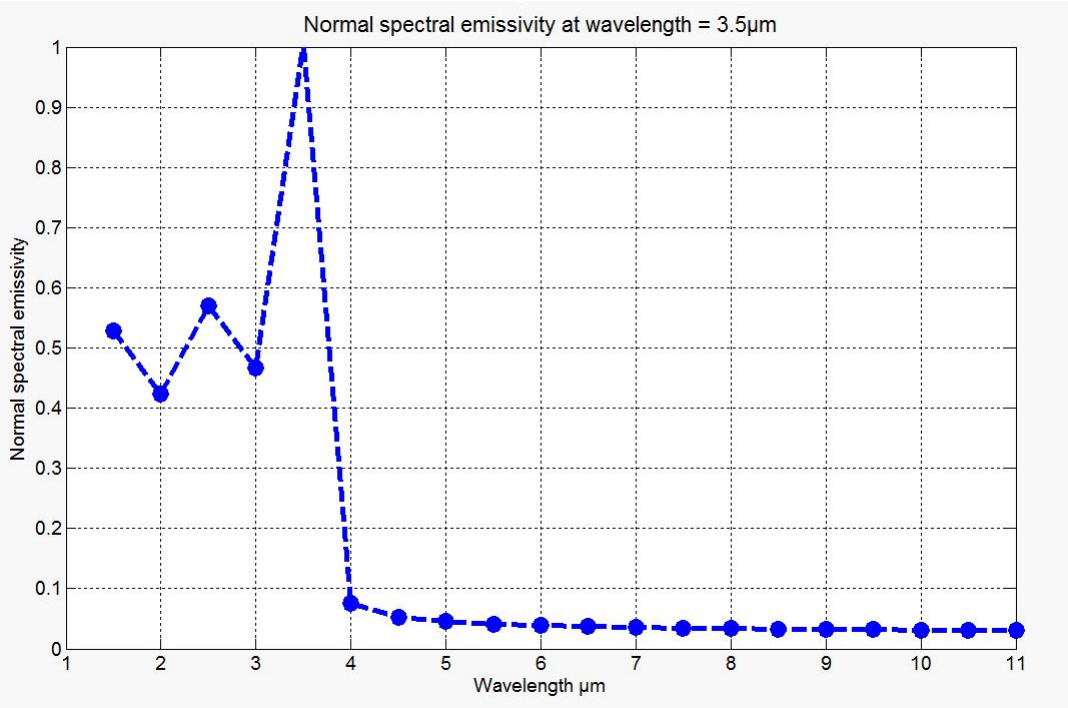

Figure 3.10: Plot of normal spectral emissivity for tantalum cylindrical cavity photonic crystal providing near unity emissivity at $\lambda \sim 3.5\mu$m. The diameter and the depth of the cylindrical cavities are $2r = 2.10\mu$m and $d = 16.0\mu$m respectively.

3.2.2 Thin layer instead of bulk tantalum

From the previous simulation, we see that the design of the tantalum photonic crystal optimized to provide a peak emissivity at a wavelength of 3.5μm has a diameter equal to 2.10μm, depth = 16μm and period 2.10μm. However, tantalum being very hard and chemically inert is very challenging to machine at micron scale. Hence, we carry out an alternate simulation to suggest an easier method to fabricate tantalum photonic crystal.

The simulation domain for this new case is shown in Figure 3.11. The inlet port and the boundary conditions of the domain is the same as the previous case. The difference here is that instead of using bulk tantalum, as with the previous case, we

use a thin layer of approximately 25 nm of tantalum on top of silicon. The dimension of the cavity and the period of the photonic crystal still remains the same as we obtained from the previous simulation. The result of the spectral plot of the new simulation is shown in Figure 3.12.

It is clear that there is no difference in the emission pattern from this new photonic crystal design and the one using bulk tantalum. The reason for this can be explained thus: Since the absorption of the incident electromagnetic waves, as described previously, happens within the skin depth of the metal. The underlying layer of tantalum does not play any role in the absorption phenomenon. So the underlying layers can be replaced with silicon or some easily machinable materials. The skin depth of tantalum in this frequency range is around 10 nm. So the new photonic crystal design with 25 nm of tantalum layer, with identical design, provides no difference in emissivity.

Apart from the advantage provided in the ease of fabrication, the new design provides a significant reduction in the overall weight of the photonic crystal structure.

3.2.3 Verifying the simulation

To verify the correctness of the simulation, a plane wave is launched at the metallic surface at various polar (θ) and azimuthal (ϕ) angles from a port defined at boundary 13. Boundary conditions are periodic along the lateral boundaries (i.e., 11, 10, 20, and 16 as shown in Figure 3.13) to simulate the metal tantalum surface. The directional spectral reflectivity $\rho(\theta, \phi, \lambda, T)$ is determined by integrating the net power flow across a surface close to and parallel to the metal for various polar(θ) and azimuthal (ϕ) angles. The directional spectral emissivity $\varepsilon(\theta, \phi, \lambda, T)$ can be then determined with $\varepsilon + \rho = 1$ and based on Kirchhoffs law for directional thermal radiation.

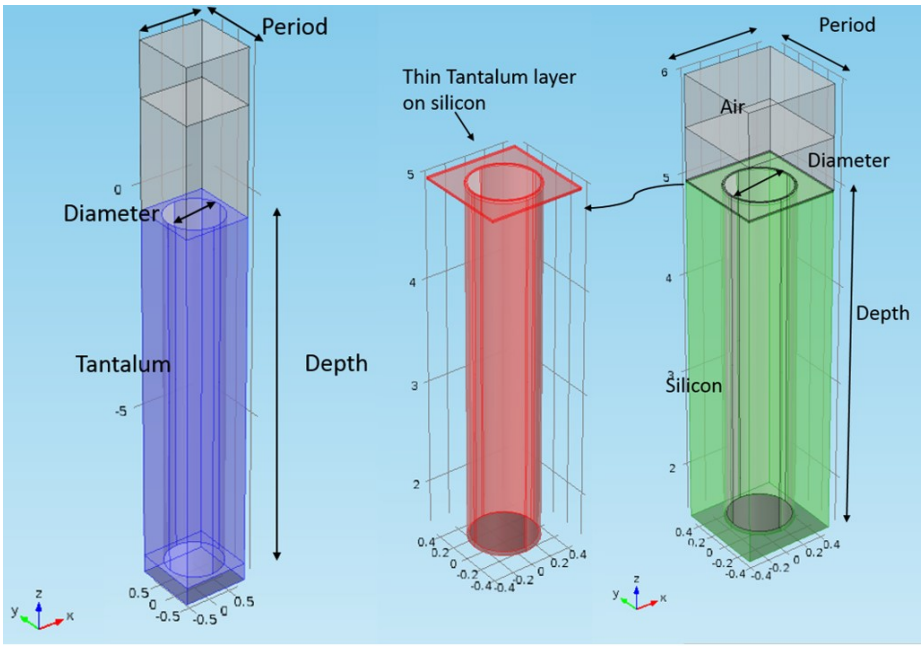

Figure 3.11: The new simulation vs old simulation domain: The old simulation used bulk tantalum is shown in blue. The new simulation uses a thin layer of tantalum layer $\sim$ 2 5nm (shown in red) on top of silicon which shown in green.

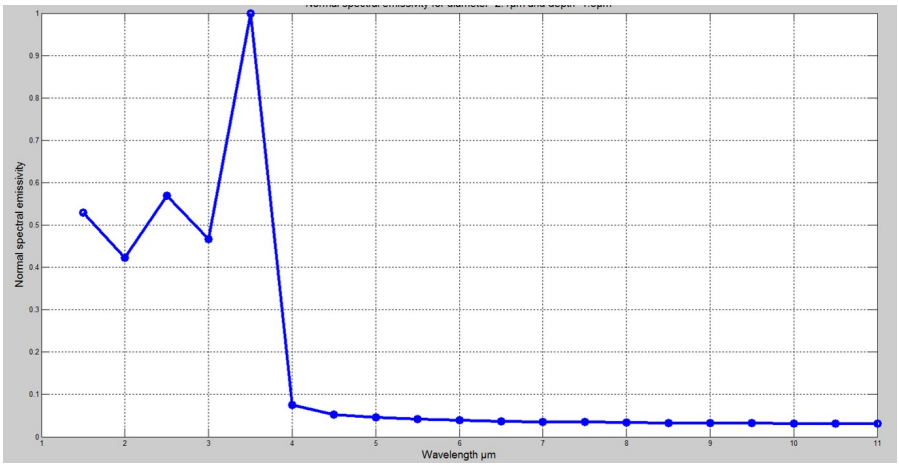

Figure 3.12: Normal spectral emissivity of the photonic crystal with a thin layer of tantalum on silicon. The dimension of the photonic crystal are still 2r = 2.10μm, d = 16μm and a = 2.10μm.

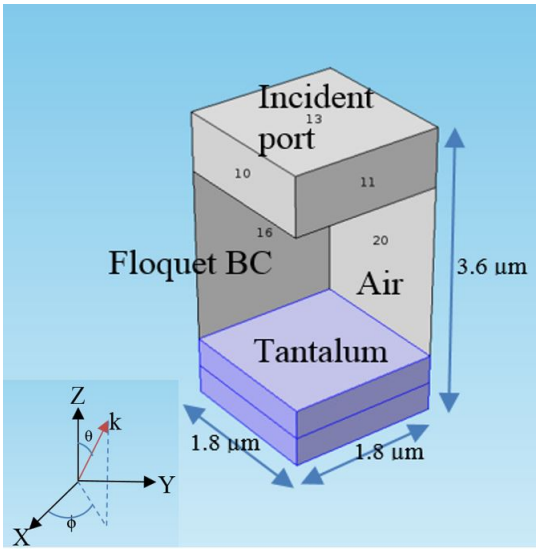

Figure 3.13: Simulation domain for flat tantalum surface (shown in blue). A plane polarized wave is launched in propagation direction $\vec{k}(\theta, \phi)$ from incident port 13. The lateral boundaries 11, 10, 20, and 16 have periodic Floquet boundary condition.

When the metal surface is flat, the directional spectral reflectivity for the S-polarized and P-polarized states, which are $\rho_S(\theta)$ and $\rho_P(\theta)$, have analytical solutions as given in [31]:

$$\rho_S(\theta, \lambda) = \frac{(n(\lambda) - \cos\theta)^2 + (\kappa(\lambda))^2}{(n(\lambda) + \cos\theta)^2 + (\kappa(\lambda))^2} \tag{3.13}$$

$$\rho_P(\theta, \lambda) = \frac{(n(\lambda)\cos\theta - 1)^2 + (\kappa(\lambda)\cos\theta)^2}{(n(\lambda)\cos\theta + 1)^2 + (\kappa(\lambda)\cos\theta)^2} \tag{3.14}$$

where $n(\lambda)$ and $\kappa(\lambda)$ are the real and imaginary part of the refractive index of the metal (i.e tantalum in this study).

Figure 3.15 shows the comparison between the analytical solutions of spectral reflectivity of tantalum at $\lambda = 2\mu$m with the numerical solutions of spectral reflectivity calcultated using COMSOL simulation. From this comparison, the error between the analytical and the numerical solutions is within 0.2%. This is a good

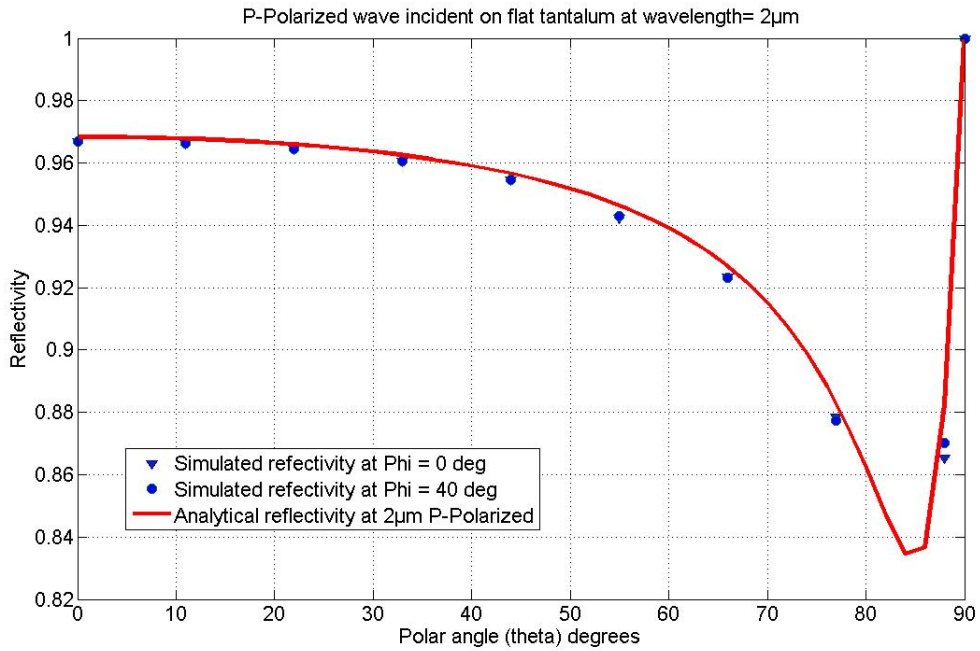

Figure 3.14: Numerical simulation vs. analytical solution of directional spectral reflectivity of P polarized electromagnetic wave of wavelength 2μm incident on a flat tantalum sheet

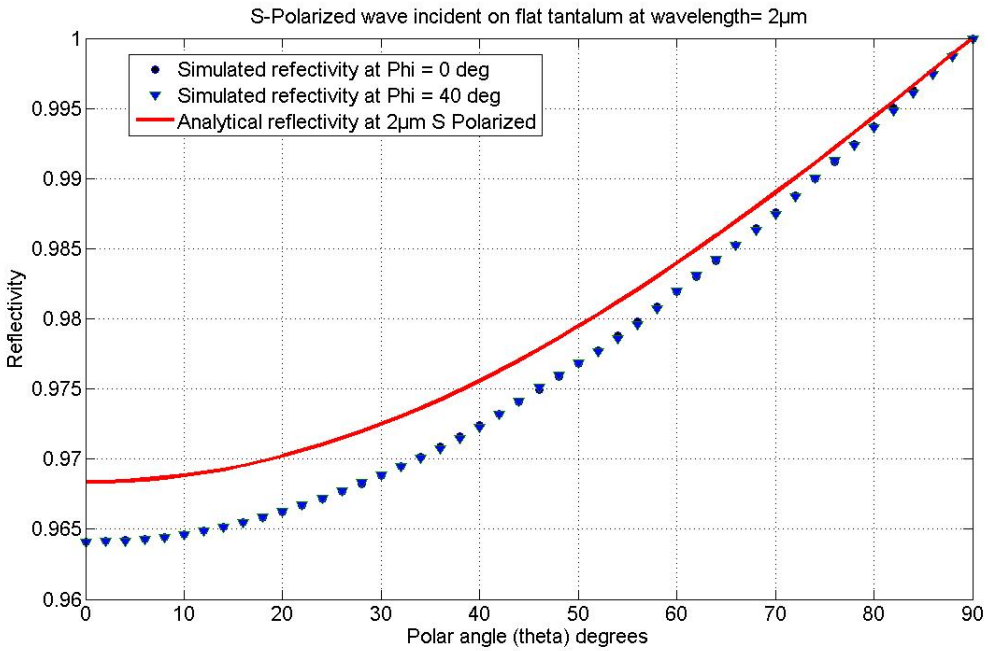

Figure 3.15: Numerical simulation vs. analytical solution of directional spectral reflectivity of S polarized electromagnetic wave of wavelength 2μm incident on a flat tantalum sheet

verification of the full wave simulation in determining the emissivity/reflectivity of metallic surfaces.

3.3 Review of current fabrication methods for 2-D photonic crystals

Electron beam lithography is a mature micro-fabrication technology. It can be used to fabricate two dimensional photonic crystals of high resolution and relatively large area. The basic fabrication processes are as follows: A layer of electron beam resist is spin coated on the substrate. Direct patterning or writing happens on the electron beam resist by accelerating electrons on to required regions. The electron beam resist undergoes chemical and physical changes when exposed to electrons. A developer can now be used to selectively react with the unexposed region and leave the exposed region intact. Thus periodic patterns could be formed of the resist layer which then can be transferred on to the subsequent layer underneath by reactive ion etching process. Electron beam lithography can provide resolutions well below 100 nm since electrons with sufficient energy can have a shorter wavelength compared to photons. Photonic crystals based on semiconductors, ferroelectric materials and organic materials can be fabricated using this technique. There is also a lot of flexibility in choosing the unit cell design. The main drawback, however, of electron beam lithography is the low throughput and cost.

Focused ion beam (FIB) method uses accelerated ion beam to etch away the material. The ion beams have even lower wavelength than the electron beams translating to higher resolutions. The sample, placed in ultrahigh vacuum, is bombarded with Ga^+ ions. The sample can be translated or rotated precisely to position it towards the beam and thus the required patterns can be generated. This technique can be even used for very hard materials like diamond.

The primary drawbacks of the FIB technique is that some material will remain

at the bottom of deep holes during the etching process, and the reflection of the ion beams off the walls of the drilled hole which is called the self focusing effect [32].

Nanoimprinting [33] is considered as an effective technology to fabricate nanometer-scale structures over large areas [34]. The technique is inexpensive and provides high throughput. An imprint stamp, which contains a reversed pattern of the surface protusions of the two dimensional photonic structure, is fabricated and imprint resin is coated on to the substrate. The pattern is then imprinted on the resin at around 120°C to generate patterns on the substrate.

The **holographic lithography** [35] or interference lithography method is a very inexpensive and useful tool to fabricate large area periodic lattice two dimensional photonic crystals and two dimensional photonic crystals.Three laser beams are required to generate a two dimensional interference pattern using the holographic lithography method. This method is very similar to the method mentioned in section 2.2.

3.4 Fabrication of 2-D metallic thin film photonic crystal

The fabrication of two dimensional photonic crystals is done using a combination of e-beam lithography, e-beam deposition and deep reactive ion etching (DRIE) at the Aggiefab facility at Texas A&M University. The fabrication process is schematically illustrated in Figure 3.16.

The fabricated area is a rectangle of dimension 1 mm $\times$ 2 mm. The direct writing of the patterns (a square array of circles) was done using electron beam (e-beam) on a (100) silicon wafer coated with a bi-layer of e-beam resist; 40 nm Hydrogen silsesquioxane(HSQ) on 280 nm thick Poly(methyl methacrylate) or PMMA [36]. The second layer of PMMA act as a buffer layer for HSQ. The buffer layer will conduct the electrons passing through the HSQ, thus preventing back scattering and

enhancing the pattern definition. Then, the development of the e-beam exposed region was done using a 4% aqueous solution of Tetramethylammonium hydroxide (TMAH).

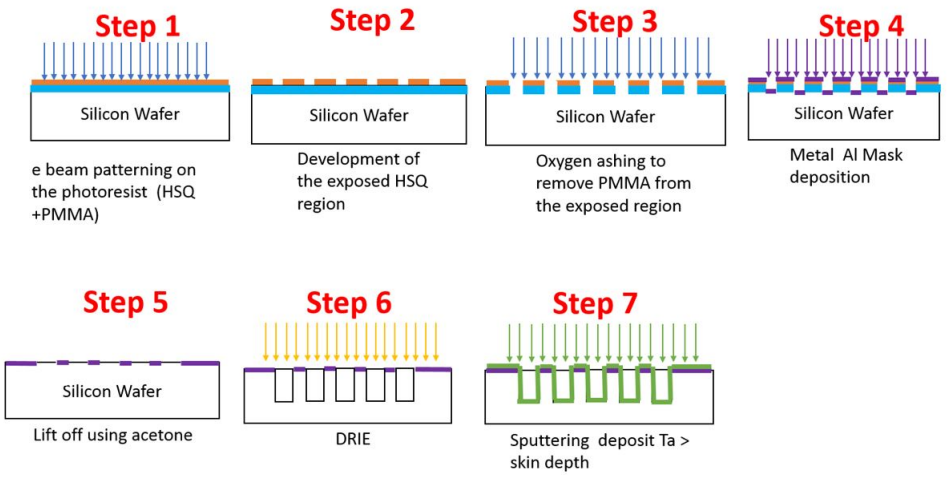

Figure 3.16: Steps employed in the fabrication of the tantalum photonic crystal. Hydrogen silsesquioxane (HSQ) and Poly(methyl methacrylate) or PMMA are electron beam resists. Deep reactive ion etching (DRIE) creates cylindrical cavities in silicon.

The region now exposing the organic polymer PMMA was then ashed away using an oxygen plasma leaving only pillars of HSQ on PMMA. Figure 3.17 shows optical image of the developed region after development and after the oxygen plasma ashing. A layer of 200 nm thick aluminum was deposited on the sample using e-beam evaporation. A directional undercut was intentionally provided on the HSQ PMMA pillars so that the lift off can be done easily.Following this, the lift off of aluminum was done from the areas with PMMA/HSQ underneath using N-Methyl-2-pyrrolidone (NMP). Figure 3.19 shows the scanning electron microscopy (SEM) micrograph of the sample before and after the lift off. Now using the aluminum as a mask, DRIE of the

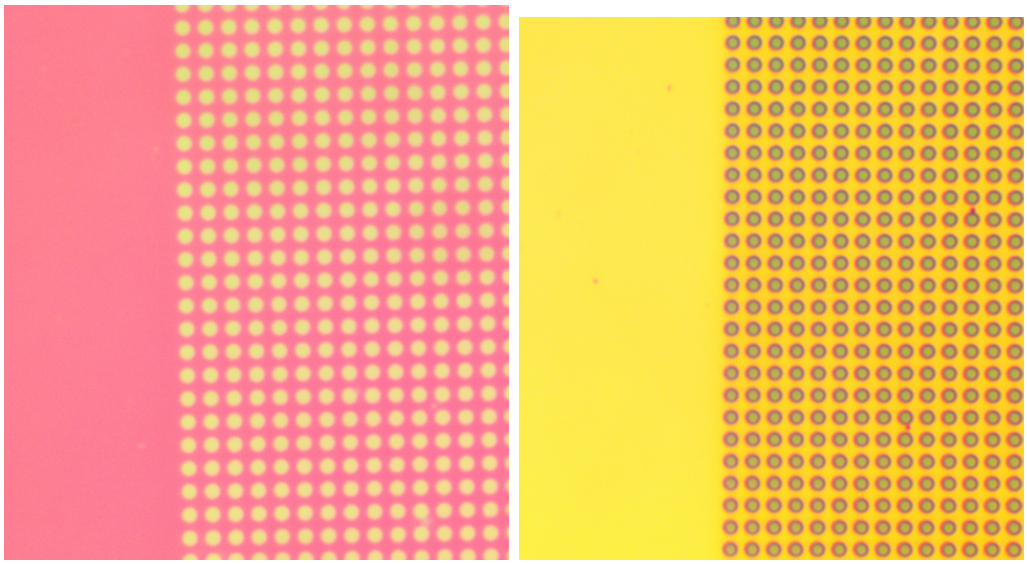

Figure 3.17: Optical images of a region of the sample. Left: after development, the violet region is the PMMA and the blue dots are the HSQ. Right: after the oxygen plasma ashing, the yellow region is the silicon and blue dots are the HSQ.

exposed silicon layer was carried out using SF_6/O_2 plasma. Intensive coupled plasma and helium backing was used to get a highly anisotropic etching to depths of ≈ 7 μm. The etching results are shown in SEM micrograph shown in Figure 3.20. This was followed by e-beam deposition of tantalum on to the surface of the sample to get the two dimensional tantalum photonic crystal.

Since the fabrication process does not rely on machining bulk tantalum but instead on depositing tantalum above a thickness greater than the skin depth ($\sim$ 10 nm for $\lambda = 3.5$ μm), the two dimensional tantalum photonic crystal obtained by this process will be lighter than those obtained by conventional methods. Moreover, anisotropic etching of silicon is easier than etching tantalum metal.

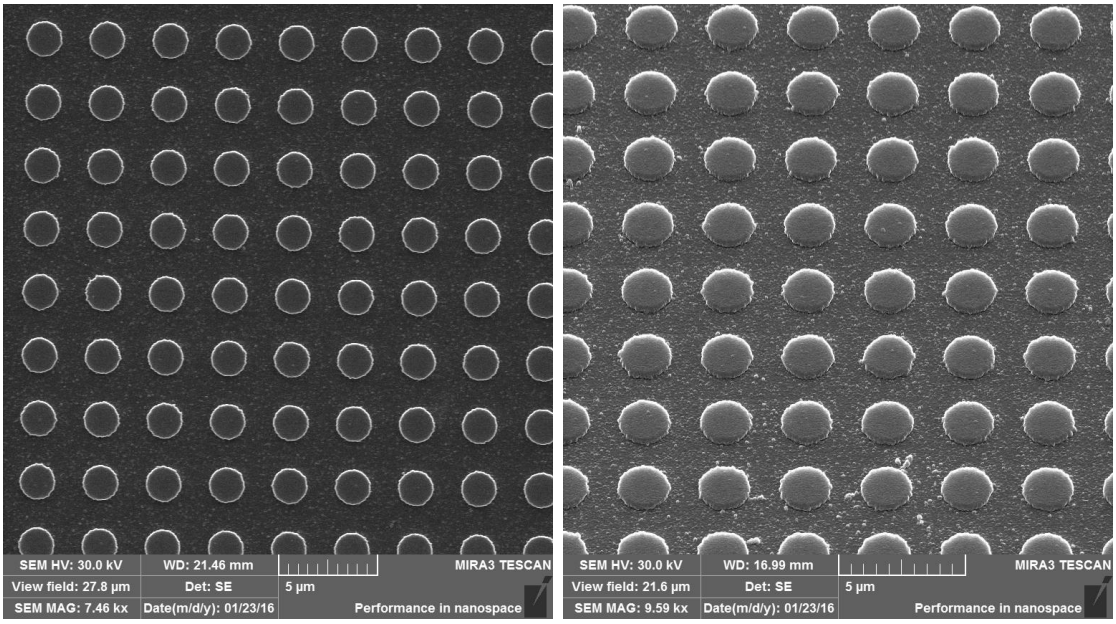

Figure 3.18: SEM images after 200 nm of aluminum deposition. Left: Normal view. Right: When viewed at 35° to the normal.

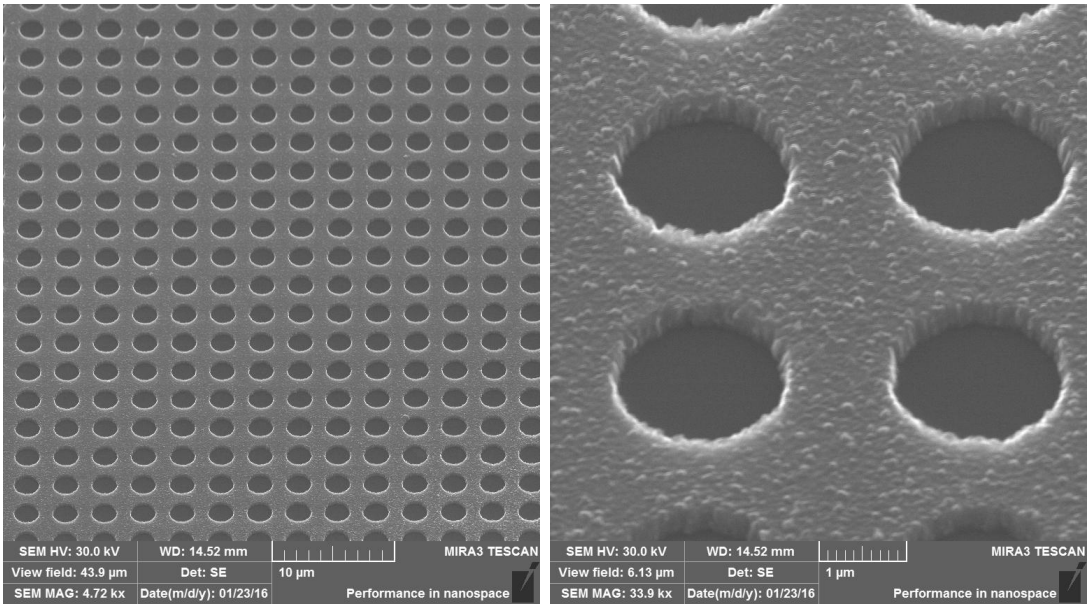

Figure 3.19: a) SEM images of the metallic photonic crystal sample after lift off. Left: Viewed at 35°. The image is taken at a magnification of 5000x and the view field is $\sim 45\mu$m. The diameter of the cavity is $\sim 2\mu$m and the period is 3.15μm. Right: Magnified image of the lifted off region at 34kx and field of view is $\sim 6\mu$m.

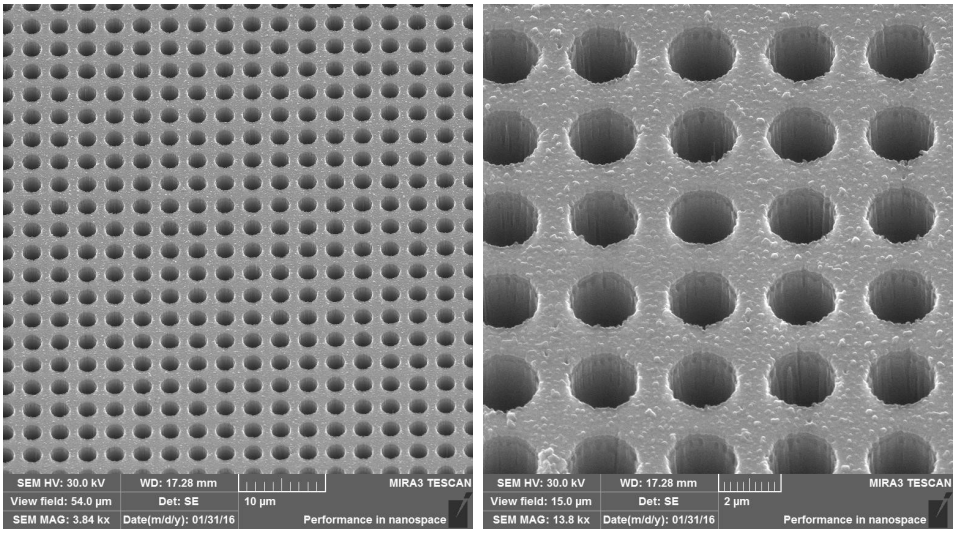

Figure 3.20: SEM images of the sample after DRIE. Left: Viewed at 35°. The dark circles in the image are the cavities. The image is at a magnification of 4000x and the view field is 55 μm. The diameter of the cavity is 2 μm and the period is 3.15μm. Right: Magnified image of the cylindrical cavity at 14kx and field of view is 17μm.

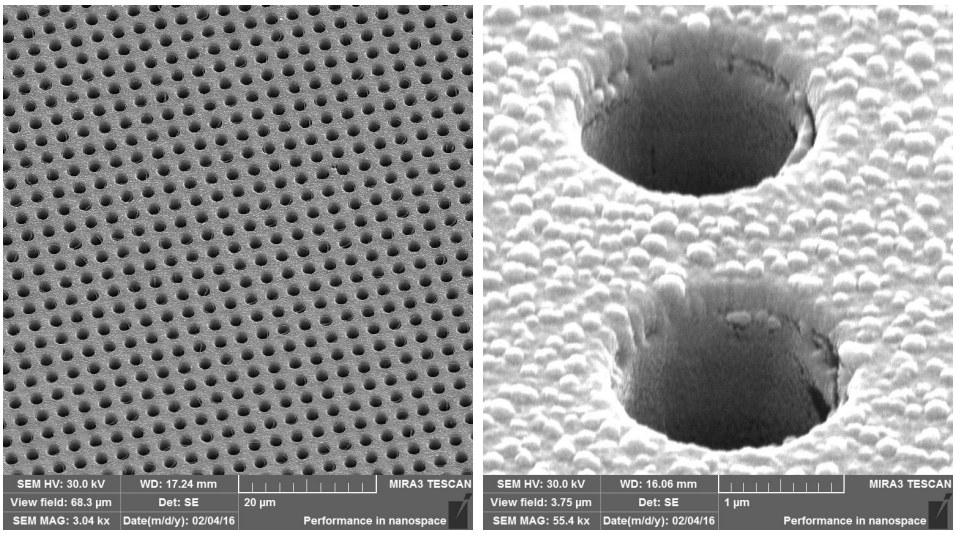

Figure 3.21: SEM images of the metallic photonic crystal after deposition of tantalum. Left: Normal View. The dark circles in the image are the cavities. The image is taken at a magnification of 3000x and the view field is $\sim$ 70 μm. The diameter of the cavity is $\sim$ 2μm and the period is 3.15 μm. Right: Magnified image of the cylindrical cavity at 55kx and field of view is $\sim$ 4 μm.

4. META SURFACE BASED PERFECT ABSORBERS

4.1 Metamaterials

Metamaterials are purposely engineered, composite materials designed to provide electromagnetic properties (permittivity and permeability) that are otherwise not attainable with natural materials [37]. The properties of the metamaterials are derived not from their chemistry but from their sub-wavelength scale geometry. This provides us high flexibility in the design of these materials with the design.

Compared to 2-D metallic photonic crystals, metamaterial-based absorbers have the ability to provide omnidirectional, polarization independent and broadband absorptivity. Fabricating metamaterial-based planar absorbers are easier in comparison with fabricating cavity type metallic photonic crystals as there is no need for high aspect ratio (length:diameter) cavities. Another advantage of metamaterial-based planar absorbers is the flexibility extended in the choice of constituents. Unlike the specific requirement to choose a metal that has high absorptivity in the wavelength of interest in 2-D metallic photonic crystals, metamaterials rely mostly on the geometry of the metal-dielectric combination.

In the previous discussion about photonic crystals, the length scale involved was nearly of the order of the wavelength of light. Now, for metamaterials the characteristic length scale is smaller than that of the photonic crystal and is approximately about a quarter of the wavelength or smaller. So the periodicity is too small to effect the wave scattering and hence, we need to investigate the effect of the electric and magnetic fields which constitute the wave.

The fields from the incoming wave will induce oscillating currents inside the metallic structures of the metamaterials which then re-emit electromagnetic waves that

combine with the applied waves resulting in interesting responses. These oscillating currents will imitate a kind of an atomic resonance and hence these metamaterials are known as resonant metamaterials.

Metamaterials have allowed the demonstration of many fascinating electromagnetic phenomena like invisibility cloaking [38], perfect lens [39], negative refractive index [40] and has inspired many exciting and potential applications. While fabricating 3D bulk metamaterials is still a challenge especially in the optical regime (400 nm to 800 nm), planar metamaterials: metasurfaces, offer an alternative option to accomplish some of these functionalities [13].

As mentioned in the first chapter, another way to achieve perfect light absorption is by using metasurface perfect absorbers. Metasurface perfect absorbers with much smaller thickness than the operational wavelength find applications as infrared detectors [41], selective emitters [42] and in thermal management [43]. They are also interesting since metasurface absorbers can also provide polarization independent, broadband absorption and even dynamically reconfigurable band [44] absorption.

In this chapter, we will qualitatively explain how a metasurface electromagnetic absorbers work, investigate different designs of metasurface absorbers and how to obtain broadband emission/absorption using these metasurface absorbers. Like in the previous chapters we will be employing full wave simulations of the Maxwell's equation to analyze the different designs.

But before we delve into metamaterials, first, we need to understand the dielectric response of the ordinary materials. Why does a material have a dielectric response or a magnetic response that we know of? This can be explained using the Lorentz model for a dielectric material and the Drude model for metals.

At equilibrium, an atom inside a dielectric material will have a symmetric distribution of the electron clouds around the nucleus. When an electric field is applied,

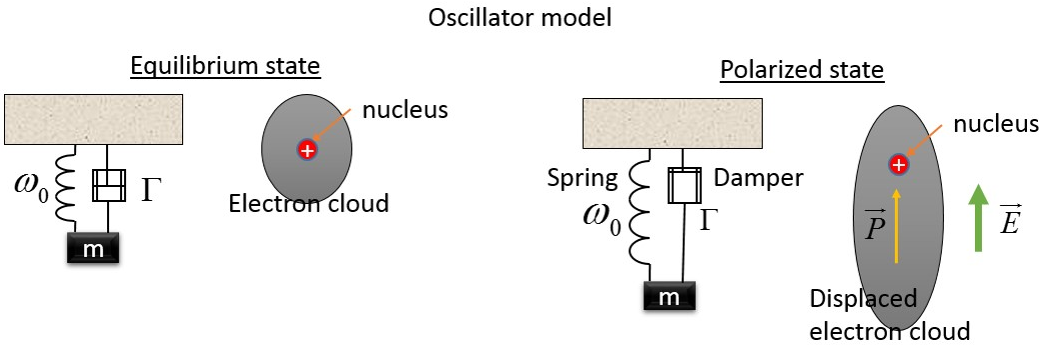

Figure 4.1: An oscillator model of the atom: At equilibrium the electron clouds are symmetrically distributed around the atom. An applied electric field $\vec{E}$ leads to the displacement of the electron clouds and create a polarization $\vec{P}$

the electrons inside the atom are displaced from their mean position relative to the nucleus. These offset charges create an electric dipole moment and a material polarization (shown in Figure 4.1) and this effect is averaged over 10^{23} atoms. This displacement of the electron cloud under the effect of the electric field can be modeled like the displacement from the mean position of a mass spring damper system.

$$m\frac{d^2\vec{r}}{dt^2} + m\Gamma\frac{d\vec{r}}{dt} + m\omega_0^2\vec{r} = -e\vec{E} \tag{4.1}$$

The resulting dielectric function can then be given by:

$$\varepsilon_r(\omega) = 1 + \frac{\omega_p^2}{(\omega_0^2 - \omega^2 + j\omega\Gamma)} \tag{4.2}$$

where the quantity $\omega_p^2 = \frac{Ne^2}{\varepsilon_0 m}$ is the plasma frequency of the dielectric material, ω_0 is the natural frequency of the system and ω is the forcing frequency. A plot of the real and imaginary part of the dielectric function is shown in Figure 4.2. There are two key points to note from the figure: 1) after ω_0 the natural frequency of the system

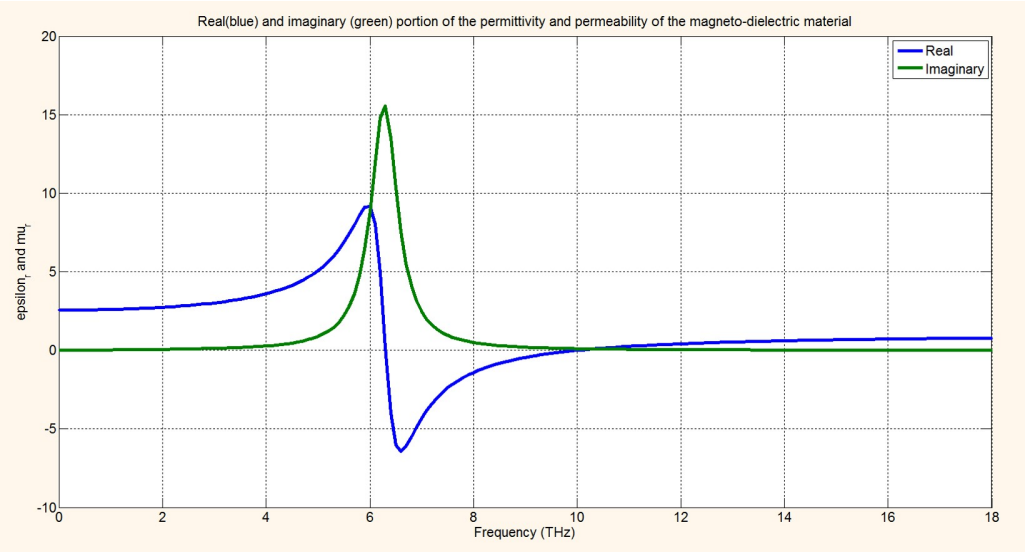

Figure 4.2: The plot of real and imaginary potion of ε and μ

ω_0 the real part of the permittivity becomes negative, and 2) there is a maximum for the imaginary part of the permittivity at ω_0. A high value of imaginary part of the permittivity translates to a high absorption of the incident radiation at that frequency.

When the applied electric field is removed, the electron cloud oscillates like a mass on the spring mass damper system and return to its mean position. During these oscillations the electron emits radiation. This electromagnetic radiation will combine with the incident electromagnetic radiation over all the atoms present in the material and produce a dielectric response.

A similar reasoning can be offered to understand the magnetic response of a material. An electron rotating around a nucleus will create a magnetic dipole moment. In the equilibrium state of the material, these magnetic dipoles are randomly arranged and thus on average there will be no net magnetic field in the material. However, when an external magnetic field is applied, all the magnetic dipoles in the

medium will align with the external magnetic field. When the external magnetic field is removed the magnetic moments will oscillate back to its original state. During this process, the electrons will re-emit radiation. This secondary radiation can combine with the incident electromagnetic wave to produce the magnetic response of the material. Again, the response can be very closely modeled as a second-order response (the displacement from equilibrium under the effect of a conservative force field can be expanded using Taylor series expansion to see this) and the magnetic permeability of the material can be given by:

$$\mu_r(\omega) = 1 + \frac{\omega_{mp}^2}{(\omega_{m0}^2 - \omega^2 + j\omega\Gamma_m)} \tag{4.3}$$

The plot of real and imaginary part of the permeability is shown in Figure 4.2. At the point corresponding to the natural frequency of oscillation, the real part of the permeability changes sign and the imaginary part has a local maximum.

At the atomic scale, metals can be considered as periodic nuclear cores surrounded by a sea of electrons. For metals, the Drude model can be considered as an extension of the Lorentz model for the dielectric material with no restoring force term. Then, the previous equation, Eq. 4.1, will reduce to:

$$m\frac{d^2\vec{r}}{dt^2} + m\Gamma_m\frac{d\vec{r}}{dt} = -e\vec{E} \tag{4.4}$$

And the permitivity is given by the simple formula:

$$\varepsilon_r(\omega) = 1 - \frac{\omega_p^2}{(\omega^2 - j\omega\Gamma)} \tag{4.5}$$

A plot of the real and imaginary part of the permittivity of the metal is shown in Figure 4.3. Here the plasma frequency $\omega_p^2 = \frac{Ne^2}{\varepsilon_0 m}$ has a physical interpretation; below

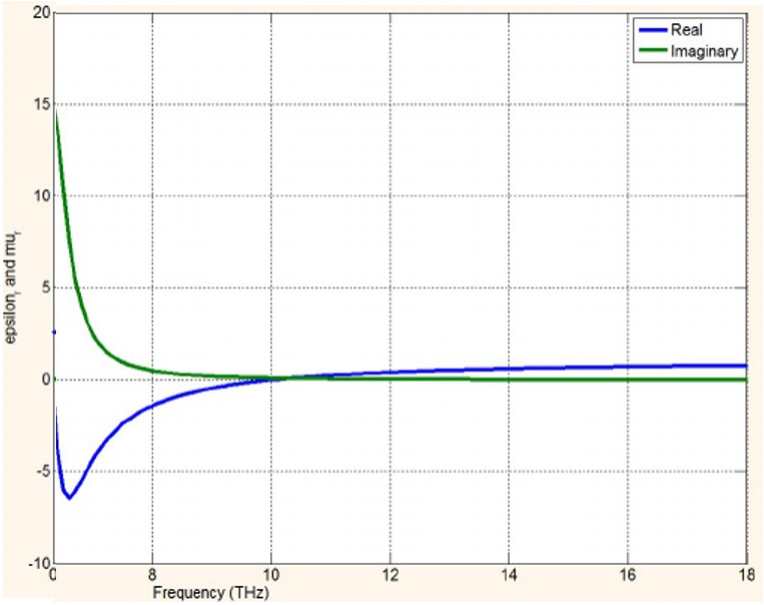

Figure 4.3: The plot of real and imagninary potion of epsilon and mu for a metal behaving according to Drude model for metal

the plasma frequency, metals (as seen before) are very lossy and the imaginary part of the permittivity is very large. And therefore, the incident electromagnetic radiation is absorbed within the skin depth. However, above the plasma frequency, metals are essentially transparent to electromagnetic radiation. The plasma frequency of common metals are of the order of few 1000 THz.

In summary, the electromagnetic response of ordinary materials are the averaged result of Avogadro number of atomic scale electric and magnetic resonances.

With this in mind, let us turn towards metamaterials. A metamaterial design by Smith et al [45] is shown in Figure 4.4. The design consists of a thin layer of copper on FR4 dielectric substrate. The incident electromagnetic radiation, which in this case is in the microwave, will create oscillating currents in the copper layer. The charges accumulating in the gap g between two metals will form a capacitance and the time varying current in the copper along the circumference will create a

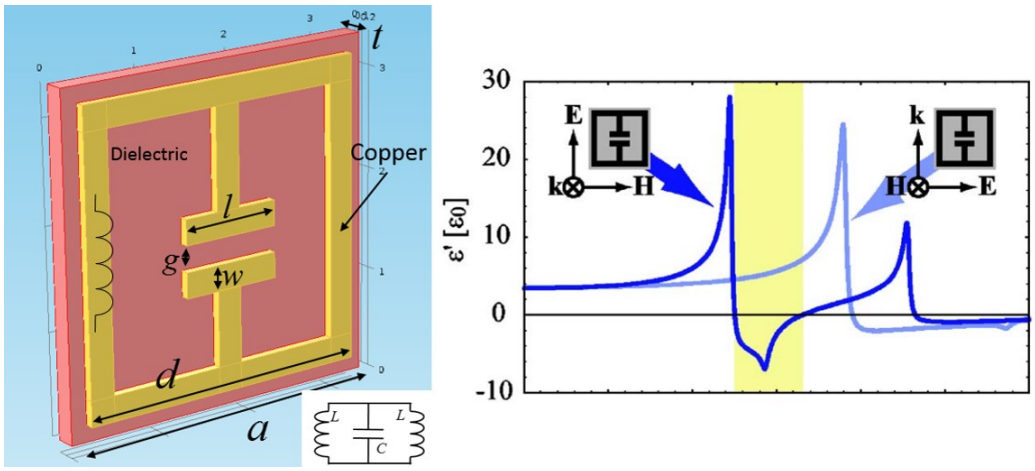

Figure 4.4: An electric ring resonator or an electric LC resonator with copper stripes on FR4 dielectric. The gap g at the center provides a capacitance and two loops create an inductive effect. The equivalent circuit is shown in inset. The dielectric response of such an ERR for different polarization is shown on right.

voltage drop and these two loops act as an inductance. Thus, the structure can be characterized as an LC resonator circuit as shown in Figure 4.4 [45]. Such a metamaterial construction is known as an Electric Ring Resonator (ERR) or an Electric LC resonator (ELC). This LC resonator circuit in its fundamental mode $\omega_0 = \sqrt{\frac{2}{LC}}$ will couple strongly to incident electric field and almost negligibly with the incident magnetic field. The electric response of such a ERR is shown in Figure 4.4 [45]. The direction of oscillation of the incident electric field (polarization) will determine the electric response of the system. When the direction of the electric field is perpendicular to the parallel face of the capacitance there is a better coupling of the incident wave and hence strong resonance. Note that this is very similar to the response of an ordinary dielectric material we discussed earlier. However, the emphasis here is that we can now vary the design parameters and in fact tune the location of resonance. Thus, we can control the dielectric response of such a structure. The imaginary part will again have a peak corresponding to the zero of

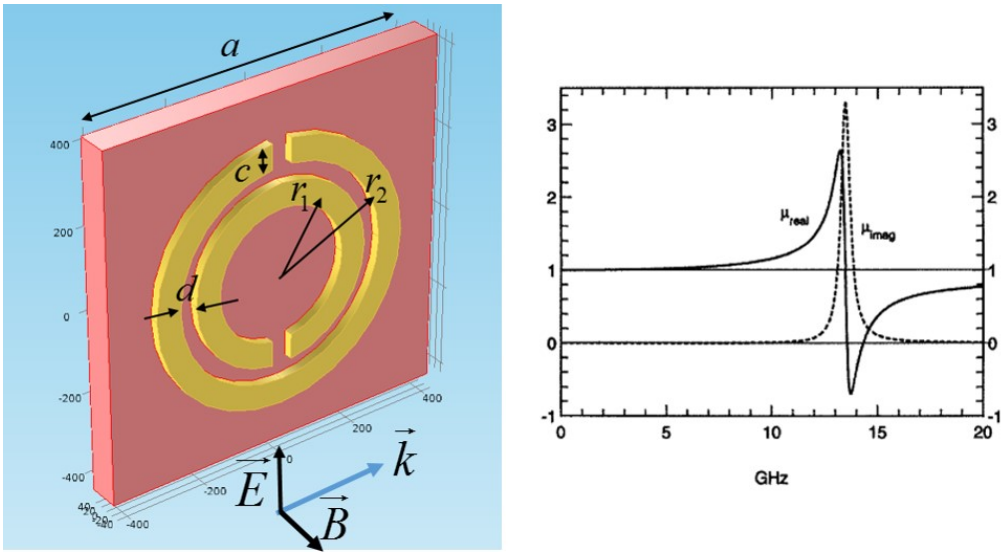

Figure 4.5: Split ring resonator (SRR) with two dielctric split rings of copper on a dielectric is shown. The SRR couples with the magnetic field of the incident wave as depicted. The real and imaginary part of the magnetic permeability is shown on the right.

the real part of the permittivity. This can be understood from the Kramers-Kronig relations which relate the real and imaginary part of the refractive index.

To understand how we can control the magnetic response, we investigate a second design which is commonly known as a Split Ring Resonator (SRR). This structure was proposed by Sir John Pendry of the Imperial College, London and the design consists of a two circular split rings as shown in Figure 4.5. The structure consists of two circular split ring on a dielectric. Pendry *et al* in [46] showed that the magnetic response of such a material can be very similar to Lorentz response as shown in figure 4.5.

A plane electromagnetic radiation at suitable frequency incident on the structure with the magnetic field polarization perpendicular to the plane of the ring will be able to couple to the resonant frequency of the Split Ring Resonator (SRR). The resonance

of the split ring can again be explained using LC analogy. The varying magnetic field will induce currents in the circular metal layer. The gap at the split ring and the gap along the circumference will create a capacitance and varying currents will produce an inductive effect making this a tunable LC circuit. The various geometric parameters can be varied to produce the required magnetic resonance.

The discussions of the previous two paragraphs shows us that we are able to engineer artificial permittivity and artificial permeability by using electric LC designs (ELC) and split ring resonators (SRR), respectively. The major difference here, from that of the natural material, is that the electric and magnetic responses are resulting not from the atomic resonance but from the sub-wavelength scale inductance and capacitance design.

Now that we can control the artificial permittivity and permeability, we can combine both to get an overall electromagnetic response. By changing the electric or magnetic resonances independently, it is possible to completely absorb the incident electric and magnetic field. Additionally, by matching ε and μ, a metamaterial can be impedance-matched to free space and thus reducing the reflectivity.

4.2 Metasurface perfect absorbers: general structure

As detailed in the previous section, metamaterials allow for the explicit design of the electric permittivity $\varepsilon(\omega)$ and magnetic permeability $\mu(\omega)$. Using these two building blocks for magnetic and electric response, one may design them each independently, and then combine them together.

The general structure of a metasurface perfect absorbers consists of three layers as shown in Figure (4.6): two metallic layer and a dielectric layer in between. The top layer forms the electric ring resonator (ERR) which along with the dielectric layer beneath provides a Lorentz-type electric response by coupling strongly to incident

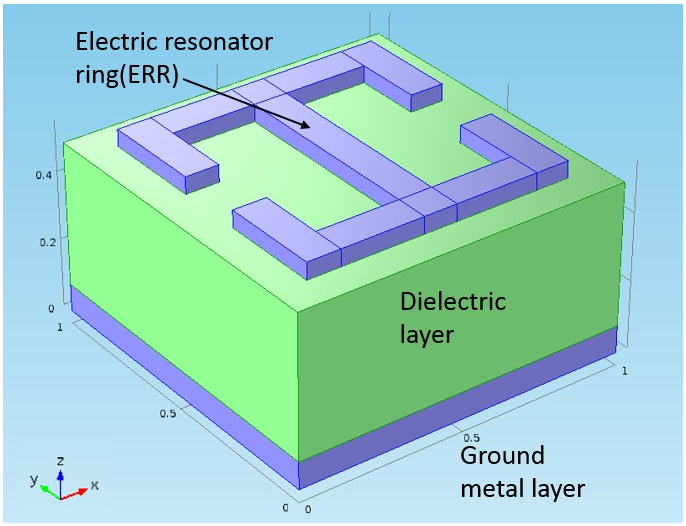

Figure 4.6: A general configuration of the metasurface perfect absorber. The top layer contains the electric ring resonator which couples with the incident electric field and the anti-parallel currents in the top and bottom metals layers generate a magnetic response

electric field at a certain resonance frequency. The ground metal layer, spaced apart from the top metal layer by a dielectric in a parallel plane, contributes to the magnetic response. The coupling of the magnetic field is achieved through anti-parallel currents in the top and ground plane of the ERR. An incident magnetic field of the electromagnetic radiation could couple to these anti-parallel currents, thus providing a Lorentz-type magnetic response. The design of the ERR and SRR allows for individual "tuning" of the electric and magnetic responses.

Electromagnetic wave incident on metasurface may be reflected, transmitted, absorbed, scattered, or may excite surface electromagnetic waves. If we consider that the average roughness (R_a) of the surface is much smaller than the wavelength λ_0 i.e. $R_a << \lambda_0$, there will be negligible scattering. If the surface electromagnetic waves die out before re-scattering back, then the incident electromagnetic wave is either reflected (R), transmitted (T) or absorbed (A), in other words A+R+T=1.

Consider a slab of metasurface of thickness d and described by a magnetic permeability $\mu(\omega) = \mu_0\mu_r(\omega)$ and the electric permittivity $\varepsilon(\omega) = \varepsilon_0\varepsilon_r(\omega)$ backed by a highly conducting metallic ground plane, then the transmittance (T) is equal to zero. ε_0 and μ_0 are the permittivity and permeability of free space.

The reflectivity (R, ratio of the reflected power to the incident power) and reflection coefficient (r, ratio of reflected electric field to incident electric field) at the interface between vacuum and the magneto-dielectric material can be obtained by solving the Maxwell's equation noting that the tangential electric fields and normal magnetic fields are the same across the interface and the expressions for the transverse electric (TE) and transverse magnetic (TM) polarized waves are given as [47]:

$$R_{TE} = |r_{TE}|^2 = \left| \frac{\mu_r \cos\theta - \sqrt{n^2 - \sin^2\theta}}{\mu_r \cos\theta + \sqrt{n^2 - \sin^2\theta}} \right|^2 \tag{4.6}$$

$$R_{TM} = |r_{TM}|^2 = \left| \frac{\varepsilon_r \cos\theta - \sqrt{n^2 - \sin^2\theta}}{\varepsilon_r \cos\theta + \sqrt{n^2 - \sin^2\theta}} \right|^2 \tag{4.7}$$

where θ is the angle of incidence and the refractive index of the magneto-dielectric medium n=$\sqrt{\mu_r\varepsilon_r}$. Note that we can separate entire electric filed into transverse electric and transverse magnetic case because all the other polarization can be formed by combination of these two. If we consider the normal incidence, i.e. $\theta = 0$, then:

$$R = \left| \frac{Z - Z_0}{Z + Z_0} \right|^2 = \left| \frac{\mu_r - n}{\mu_r + n} \right|^2 \tag{4.8}$$

where $Z = \sqrt{\mu/\varepsilon}$ is the impedance of the metasurface and $Z_0 = \sqrt{\mu_0/\varepsilon_0}$ is the impedance of free space.

If the impedance is matched to that of the free space, reflectance equals zero

($Z = Z_0 \rightarrow R = 0$), transmission is zero because of the thick metal layer underneath and permittivity and permeability are tuned so as to have perfect absorption at a required frequency, we can perfectly absorb all the radiation that is incident on the metasurface (at that particular frequency). If our material is not of sufficient thickness d and lossy, then there is a probability that the wave will be reflected from the conducting metallic plane below and may be reflected back into free space. The penetration depth and thus the loss in magneto-dielectric material can be given by $\delta = c/2\omega\varepsilon_{2r}$. The ε_{2r} is the imaginary part of the permittivity. So our metal-backed magneto dielectric medium can absorb a narrow range of frequencies where the loss of our Lorentz oscillator is maximum. The discussion in the following section will be to get a broadband response.

4.3 Narrow band perfect absorbers

Even though we could independently design the electric and magnetic response of the ERR and SRR, undesirable electromagnetic interactions between unit cells will call for further optimization of the periodic structure. The combined unit cell can be modeled using the finite element scheme of the last chapter and we can design the peak absoptivity.

A perfect light absorber is a device which provides a near unity total hemispherical absorptivity for light incident on it at a particular wavelength. A perfect absorber can be achieved with metasurface composed with micro/nanoscale surface patterns. In this section, we perform a full wave simulation of a perfect light absorber based on a metamaterial constructed with sub-wavelength scale cross-shaped electric ring resonator (ERR). The reason for selecting the cross shaped electric ring resonator is that in such design, where there are four fold symmetries, the dielectric resonance becomes independent of the polarization of the incident light. A cross ring resonator is illustrated in figure 4.7 as part of an infinite array of metal ERR stacked on a thin dielectric material placed on a metal block.

The simulation domain used in the full wave analysis is illustrated in the figure 4.8. Figure 4.8 also shows the design parameters namely the width and length of the gold cross, thickness of the dielectric layer and length of the each ERR which is varied during the simulation to obtain perfect absorption at around 2μm. The dielectric material used is gallium antimonide (GaSb) [48] which has a peak absorption around 2μm. The thickness of the dielectric layer, in this simulation, is varied from 0.1μm to 0.4μm, the length of the gold cross is varied from 1μm to 2μm and the width is fixed at 0.4μm. We then carry out batch simulation to calculate the absorptivity of the metasurface absorber at various wavelength range from 0.2μm to 2.48μm.

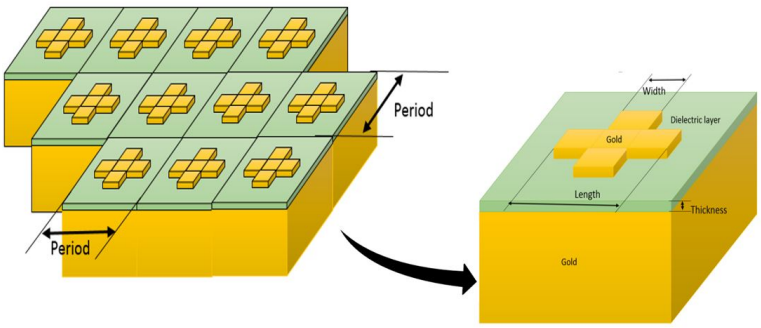

Figure 4.7: An infinite array of cross shaped electric resonators (ER) of gold on top of a thin dielectric layer (in green color). Parameters of an ER unit, namely, thickness of dielectric layer and length of the gold cross that need to be varied to achieve perfect absorption at a desired wavelength.

By adjusting the length of the gold cross and the thickness of the dielectric layer, the characteristic impedance of the metamaterial can be fine-tuned to have zero reflection at selected wavelengths (i.e., perfect absorber). The procedure to determine the required design of the electric ring resonator to achieved perfect light absorption at $\lambda = 2\mu$m is illustrated in figure (4.10). This gives the optimum thickness of the dielectric as 1.45μm and the length of the gold cross to be 0.11μm. The plot of normal spectral absorptivity for such a gold ERR is shown in figure 4.11.

Next we try to obtain broad band absorption but before that a note on the complimentary patterns is required. Figure (4.12) shows the complimentary pattern of the electric ring resonator shown before. The interesting thing to note here is that since both these metal patterns are complimentary there is no difference in the resonance characteristics of one from the other. This can be explained as: since this is a linear system(governing equation and refractive index are linear), the electric field calculated from the right pattern of figure(4.12) plus the electric field from the left should equal the electric field of a flat surface so which means the amplitude

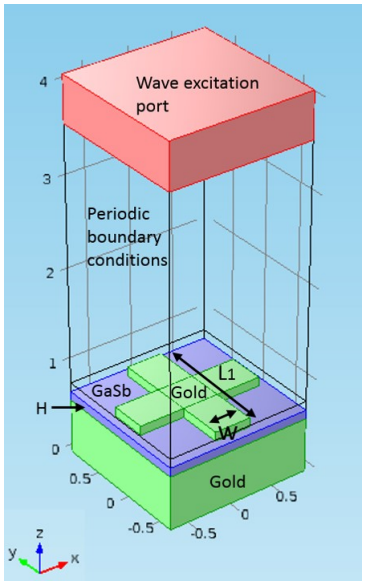

Figure 4.8: Figure 1(a) an infinitely large array of electric ring resonators (ERR) on top of a thin dielectric layer (in green color); (b) design parameters of a ERR unit, namely, thickness of dielectric layer and length of the gold cross.

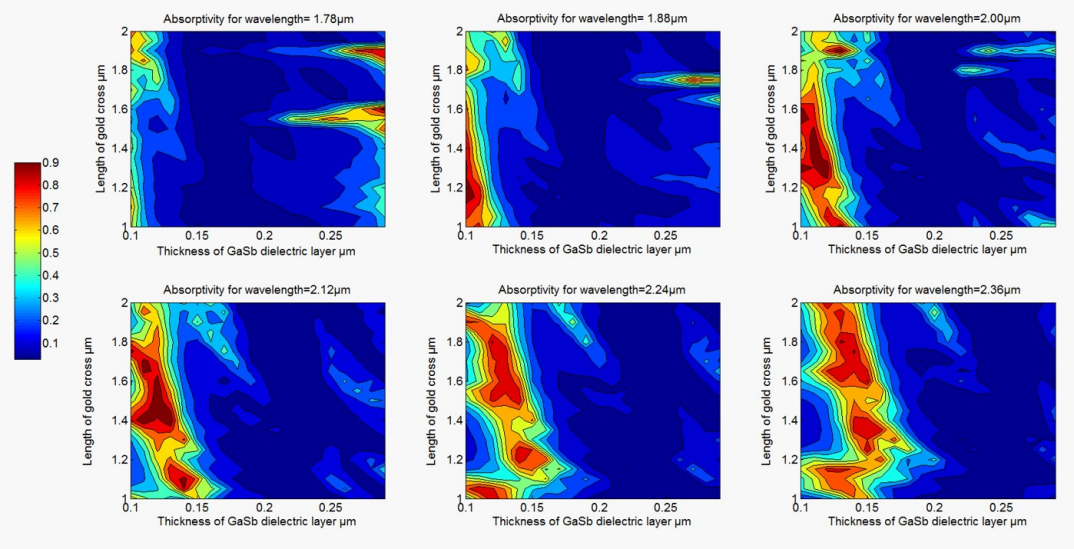

Figure 4.9: Contour plot of the absorptivity of Gold cross ring resonator a function of the thickness of the GaSb dielectric slab and length of the gold cross at each wavelength. (b) Illustration of the way to determine the optimized length of the gold cross and thickness of the GaSb for wavelength = 2m

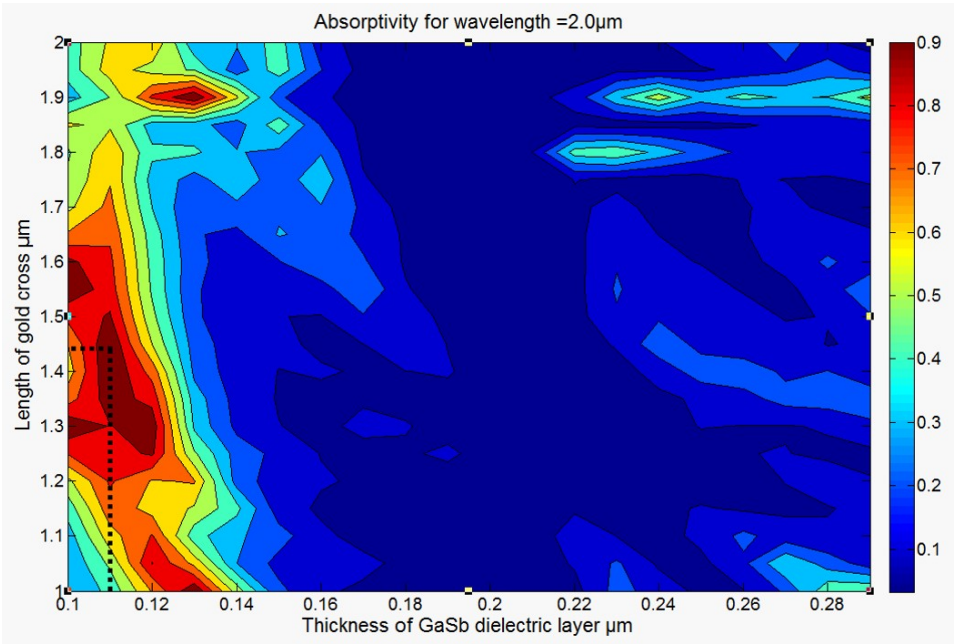

Figure 4.10: Contour plot of the normal spectral absorptivity of Gold electric ring resonator providing near unity absorptivity at 2 m. The length of the gold cross and the thickness of the GaSb dielectric layer are respectively 1.45μm and 0.11μm.

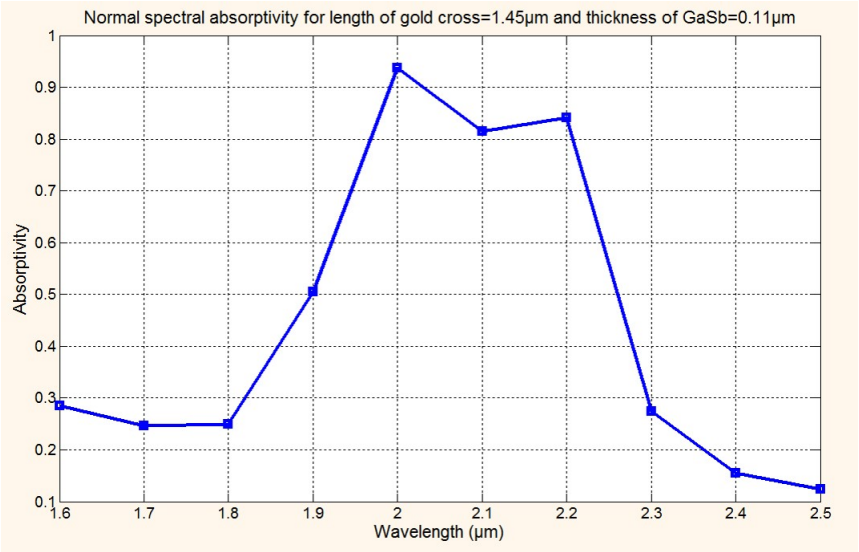

Figure 4.11: Normal spectral absorptivity of Gold electric ring resonator providing near unity absorptivity at $\lambda \sim 2\mu$m. The length of the gold cross and the thickness of the GaSb dielectric layer are respectively 1.45μm and 0.11μm.

of the electric field will be same but of opposite sign since both need to add up to zero. So when ever the pattern has an electric resonance the complimentary too has a resonance but with opposite sign. A detailed explaination of this can be done using the Babinet's principle. So the absorptivity spectrum of both these designs will be exactly the same.

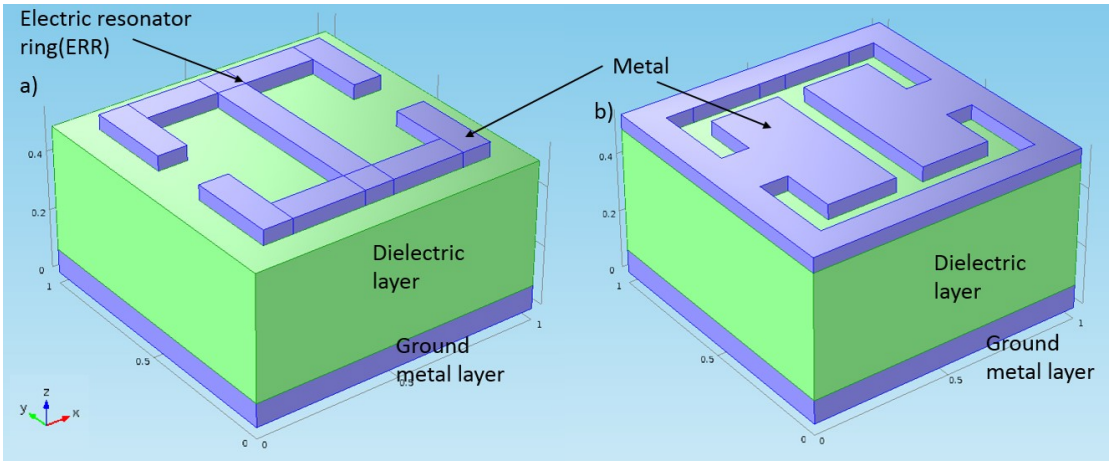

Figure 4.12: Normal spectral absorptivity of Gold electric ring resonator providing near unity absorptivity at $\lambda \sim 2\mu$m. The length of the gold cross and the thickness of the GaSb dielectric layer are respectively 1.45μm and 0.11μm.

5. CONCLUSION AND FUTURE WORK

5.1 Conclusion and future work

Perfect absorption of incident electromagnetic waves at a particular wavelength or a range of wavelengths provides a strong stepping stone for many interesting applications. For example, we could design more efficient solar panels and thermophotovoltaic conversion systems. In this thesis, we discussed in detail two important ways to realize perfect absorbers namely 2-D photonic crystals and metasurface absorbers. We answered in the second chapter of this thesis how the photonic band gaps originate. In the third chapter, we further showed that the 2-D metallic photonic crystals could absorb all the radiation that is incident on it. Then, we went on to fabricate a two dimensional metallic photonic crystal using tantalum. And in the last chapter, we showed that metamaterials provide a good alternative to 2- D photonic crystals as perfect absorbers providing broadband, omnidirectional absorption.

The applications of photonic crystals and metamaterials still continue to be very active area of research. The research over the last two decades have contributed significantly to the advancement of the communication and optoelectronics industries. Many metamaterials-based technologies are getting commercialized and companies like 'KYMETA' that develop metamaterials-based antennas are already in the market. It will not be long before metamaterials or photonic crystals will become an everyday term.

The main focus of this thesis was to show that photonic crystal and metamaterials could act as perfect absorbers. However, this is only the first step. However, there is still scope for the current work to be applied many diverse and interesting applications. We propose the following activities as our future work which will be a

natural follow up to this research:

1. Fabrication of large area 2-D metallic photonic crystal using microlithography: The fabricated photonic crystal of tantalum in the present work is of the area of nearly 2 mm^2. Techniques like electron beam lithography used will become too costly when fabricating large areas. To remedy this, we propose to fabricate a large area 2-D photonic crystal using methods like interference lithography and oil immersion lithography.

2. Measurement of the emissivity of the photonic crystal: For an accurate measurement of the emissivity of the photonic crystal we need to fabricate an area of at least 1 cm^2. With a sample of this size, we can use the UV-VIS NIR spectrophotometer with an integrating sphere to calculate the reflectance and hence, the absorptivity or emissivity. This will provide a venue to compare our experimental and simulated emissivity.

3. Another interesting future work proposed is to integrate the photonic crystal to a thermal device and then measure the energy conversion efficiency. The efficiency of conversion of thermal energy to electrical energy will be enhanced because of the tailoring of emissivity from the high temperature source by the photonic crystal to suit the bandgap of the photovoltaic cell.

4. Fabricate a metamaterial absorber with broadband absorptivity at around 2 μm: From the design arrived in chapter four, the minimum feature size required for this device would be around 200 nm. The fabrication of this device could be possible by using projection lithography using a UV light source. Integrating this to a thermal energy source and measuring the energy captured as radiation will be a good test of performance of metamaterial absorber device.

5. Since the electric resonance that is created during the absorption of light produces very high electric fields in the region between the metals. Nonlinear optical effects like 2-photon absorption could be generated using metamaterials.

6. Lastly, we would also like to fabricate 1-D photonic crystals using thin film transfer technique. This method starts with spin coating a dielectric layer on a polyelectrolyte which can be dissolved in water. The free standing film on water can be stacked on to a substrate one after another to produce a one dimensional photonic crystal. This technique will have the potential to reduce the fabrication time of conventional photonic crystal by at least one order of magnitude.

REFERENCES

[1] J. D. Joannopoulos, S. G. Johnson, J. N. Winn, and R. D. Meade, *Photonic crystals: molding the flow of light*. Princeton university press, 2011.

[2] E. Yablonovitch, "Inhibited spontaneous emission in solid-state physics and electronics," *Phys. Rev. Lett.*, vol. 58, pp. 2059–2062, May 1987.

[3] S. John, "Strong localization of photons in certain disordered dielectric superlattices," *Phys. Rev. Lett.*, vol. 58, pp. 2486–2489, Jun 1987.

[4] S. G. Johnson and J. D. Joannopoulos, "Introduction to photonic crystals: Blochs theorem, band diagrams, and gaps (but no defects)," *Photonic Crystal Tutorial*, pp. 1–16, 2003.

[5] K. Kitano, K. Suzuki, K. Ishizaki, and S. Noda, "Three-dimensional photonic crystals fabricated by simultaneous multidirectional etching," *Physical Review B*, vol. 91, no. 15, p. 155308, 2015.

[6] V. Rinnerbauer, S. Ndao, Y. X. Yeng, J. J. Senkevich, K. F. Jensen, J. D. Joannopoulos, M. Soljačić, I. Celanovic, and R. D. Geil, "Large-area fabrication of high aspect ratio tantalum photonic crystals for high-temperature selective emitters," *Journal of Vacuum Science & Technology B*, vol. 31, no. 1, p. 011802, 2013.

[7] I. Celanovic, N. Jovanovic, and J. Kassakian, "Two-dimensional tungsten photonic crystals as selective thermal emitters," *Applied Physics Letters*, vol. 92, no. 19, p. 193101, 2008.

[8] J. R. Howell, M. P. Menguc, and R. Siegel, *Thermal radiation heat transfer*. CRC press, 2010.

[9] V. Rinnerbauer, S. Ndao, Y. X. Yeng, W. R. Chan, J. J. Senkevich, J. D. Joannopoulos, M. Soljacic, and I. Celanovic, "Recent developments in high-temperature photonic crystals for energy conversion," *Energy Environ. Sci.*, vol. 5, pp. 8815–8823, 2012.

[10] V. Rinnerbauer, S. Ndao, Y. X. Yeng, W. R. Chan, J. J. Senkevich, J. D. Joannopoulos, M. Soljačić, and I. Celanovic, "Recent developments in high-temperature photonic crystals for energy conversion," *Energy & Environmental Science*, vol. 5, no. 10, pp. 8815–8823, 2012.

[11] A. K. Azad, W. J. Kort-Kamp, M. Sykora, N. R. Weisse-Bernstein, T. S. Luk, A. J. Taylor, D. A. Dalvit, and H.-T. Chen, "Metasurface broadband solar absorber," *arXiv preprint arXiv:1509.06666*, 2015.

[12] H. Tao, N. I. Landy, C. M. Bingham, X. Zhang, R. D. Averitt, and W. J. Padilla, "A metamaterial absorber for the terahertz regime: Design, fabrication and characterization," *Optics express*, vol. 16, no. 10, pp. 7181–7188, 2008.

[13] N. Landy, S. Sajuyigbe, J. Mock, D. Smith, and W. Padilla, "Perfect metamaterial absorber," *Physical review letters*, vol. 100, no. 20, p. 207402, 2008.

[14] T. Cao, C.-w. Wei, R. E. Simpson, L. Zhang, and M. J. Cryan, "Broadband polarization-independent perfect absorber using a phase-change metamaterial at visible frequencies," *Scientific reports*, vol. 4, 2014.

[15] J. D. Jackson, *Classical electrodynamics*. Wiley, 1999.

[16] N. Bloembergen, *Nonlinear optics*. World Scientific, 1996.

[17] T. Komikado, S. Yoshida, and S. Umegaki, "Surface-emitting distributed-feedback dye laser of a polymeric multilayer fabricated by spin coating," *Applied physics letters*, vol. 89, no. 6, p. 061123, 2006.

[18] J. Yoon, W. Lee, J.-M. Caruge, M. Bawendi, E. L. Thomas, S. Kooi, and P. N. Prasad, "Defect-mode mirrorless lasing in dye-doped organic/inorganic hybrid one-dimensional photonic crystal," *Applied physics letters*, vol. 88, no. 9, p. 091102, 2006.

[19] K. M. Chen, A. W. Sparks, H.-C. Luan, D. R. Lim, K. Wada, and L. C. Kimerling, "Sio2/tio2 omnidirectional reflector and microcavity resonator via the sol-gel method," *Applied Physics Letters*, vol. 75, p. 3805, 1999.

[20] G. Barillaro, A. Nannini, and M. Piotto, "Electrochemical etching in hf solution for silicon micromachining," *Sensors and Actuators A: Physical*, vol. 102, no. 1, pp. 195–201, 2002.

[21] G. Barillaro, A. Nannini, and F. Pieri, "Dimensional constraints on high aspect ratio silicon microstructures fabricated by hf photoelectrochemical etching," *Journal of The Electrochemical Society*, vol. 149, no. 3, pp. C180–C185, 2002.

[22] M. Campbell, D. Sharp, M. Harrison, R. Denning, and A. Turberfield, "Fabrication of photonic crystals for the visible spectrum by holographic lithography," *Nature*, vol. 404, no. 6773, pp. 53–56, 2000.

[23] M. Moharam and T. Gaylord, "Rigorous coupled-wave analysis of planar-grating diffraction," *JOSA*, vol. 71, no. 7, pp. 811–818, 1981.

[24] M. Moharam and T. K. Gaylord, "Diffraction analysis of dielectric surface-relief gratings," *JOSA*, vol. 72, no. 10, pp. 1385–1392, 1982.

[25] C. A. Balanis, *Advanced engineering electromagnetics*. John Wiley & Sons, 2012.

[26] W. L. Barnes, A. Dereux, and T. W. Ebbesen, "Surface plasmon subwavelength optics," *Nature*, vol. 424, no. 6950, pp. 824–830, 2003.

[27] J. Pitarke, V. Silkin, E. Chulkov, and P. Echenique, "Theory of surface plasmons and surface-plasmon polaritons," *Reports on progress in physics*, vol. 70, no. 1, p. 1, 2006.

[28] S. A. Maier, *Plasmonics: fundamentals and applications*. Springer Science & Business Media, 2007.

[29] H. A. Haus, *Waves and fields in optoelectronics*. Prentice-Hall,, 1984.

[30] M. A. Ordal, R. J. Bell, R. W. Alexander, L. A. Newquist, and M. R. Querry, "Optical properties of al, fe, ti, ta, w, and mo at submillimeter wavelengths," *Applied optics*, vol. 27, no. 6, pp. 1203–1209, 1988.

[31] T. L. Bergman, F. P. Incropera, and A. S. Lavine, *Fundamentals of heat and mass transfer*. John Wiley & Sons, 2011.

[32] A. Chelnokov, K. Wang, S. Rowson, P. Garoche, and J.-M. Lourtioz, "Near-infrared yablonovite-like photonic crystals by focused-ion-beam etching of macroporous silicon," *Applied Physics Letters*, vol. 77, no. 19, pp. 2943–2945, 2000.

[33] K. J. Byeon, S. Y. Hwang, and H. Lee, "Fabrication of two-dimensional photonic crystal patterns on gan-based light-emitting diodes using thermally curable monomer-based nanoimprint lithography," *Applied physics letters*, vol. 91, no. 9, 2007.

[34] J. S. Gwag, M. Oh-e, M. Yoneya, H. Yokoyama, H. Satou, and S. Itami, "Advanced nanoimprint lithography using a graded functional imprinting material tailored for liquid crystal alignment," *Journal of Applied Physics*, vol. 102, no. 6, p. 063501, 2007.

[35] G. Zito, B. Piccirillo, E. Santamato, A. Marino, V. Tkachenko, and G. Abbate, "Two-dimensional photonic quasicrystals by single beam computer-generated holography," *Optics express*, vol. 16, no. 8, pp. 5164–5170, 2008.

[36] V. Sundaram and S. Wen, "An easy method to perform e-beam negative tone lift-off fabrication on dielectric material with a sandwiched conducting polymer layer," *Journal of Micromechanics and Microengineering*, vol. 21, no. 6, p. 065021, 2011.

[37] C. M. Watts, X. Liu, and W. J. Padilla, "Metamaterial electromagnetic wave absorbers," *Advanced Materials*, vol. 24, no. 23, 2012.

[38] D. Schurig, J. Mock, B. Justice, S. A. Cummer, J. B. Pendry, A. Starr, and D. Smith, "Metamaterial electromagnetic cloak at microwave frequencies," *Science*, vol. 314, no. 5801, pp. 977–980, 2006.

[39] J. B. Pendry, "Negative refraction makes a perfect lens," *Physical review letters*, vol. 85, no. 18, p. 3966, 2000.

[40] V. G. Veselago, "The electrodynamics of substances with simultaneously negative values of and?," *Soviet physics uspekhi*, vol. 10, no. 4, p. 509, 1968.

[41] J.-Y. Jung, J. Lee, D.-G. Choi, J.-H. Choi, J.-H. Jeong, E.-S. Lee, and D. P. Neikirk, "Wavelength-selective infrared metasurface absorber for multispectral thermal detection," *IEEE Photonics Journal*, vol. 7, no. 6, pp. 1–10, 2015.

[42] D. Woolf, J. Hensley, J. Cederberg, D. Bethke, A. Grine, and E. Shaner, "Heterogeneous metasurface for high temperature selective emission," *Applied Physics Letters*, vol. 105, no. 8, p. 081110, 2014.

[43] A. P. Raman, M. A. Anoma, L. Zhu, E. Rephaeli, and S. Fan, "Passive radiative cooling below ambient air temperature under direct sunlight," *Nature*, vol. 515,

no. 7528, pp. 540–544, 2014.

[44] Y. Yao, R. Shankar, M. A. Kats, Y. Song, J. Kong, M. Loncar, and F. Capasso, "Electrically tunable metasurface perfect absorbers for ultrathin mid-infrared optical modulators," *Nano letters*, vol. 14, no. 11, pp. 6526–6532, 2014.

[45] D. Schurig, J. Mock, and D. Smith, "Electric-field-coupled resonators for negative permittivity metamaterials," *Applied Physics Letters*, vol. 88, no. 4, p. 041109, 2006.

[46] J. B. Pendry, A. J. Holden, D. Robbins, and W. Stewart, "Magnetism from conductors and enhanced nonlinear phenomena," *IEEE transactions on microwave theory and techniques*, vol. 47, no. 11, pp. 2075–2084, 1999.

[47] K. R. Demarest, *Engineering electromagnetics*.

[48] R. Ferrini, M. Patrini, and S. Franchi, "Optical functions from 0.02 to 6 ev of alxga1- xsb/gasb epitaxial layers," *Journal of applied physics*, vol. 84, no. 8, pp. 4517–4524, 1998.